POLITECNICO DI TORINO
Repository ISTITUZIONALE

Design and Comparison of Air-Core and High-Power-Density Synchronous Machines for Hybrid Electric Aircraft

Original
Design and Comparison of Air-Core and High-Power-Density Synchronous Machines for Hybrid Electric Aircraft / Perilli, L., Credo, A., Fabri, G., Graffeo, F., Tenconi, A., Vaschetto, S.. - In: ENERGIES. - ISSN 1996-1073. - 19:7(2026). [10.3390/en19071673]

Availability:
This version is available at: 11583/3013753 since: 2026-07-30T09:36:21Z

Publisher:
MDPI

Published
DOI:10.3390/en19071673

Terms of use:

This article is made available under terms and conditions as specified in the corresponding bibliographic description in the repository

Publisher copyright

(Article begins on next page)

18 November 2026

energies

MDPI

Article

Design and Comparison of Air-Core and High-Power-Density Synchronous Machines for Hybrid Electric Aircraft

Lorenzo Perilli [1,*], Andrea Credo [2], Giuseppe Fabri [2], Federica Graffeo [1], Alberto Tenconi [1] and Silvio Vaschetto [1]

[1] Dipartimento Energia "Galileo Ferraris", Politecnico di Torino, 10129 Turin, Italy; federica.graffeo@polito.it (F.G.); alberto.tenconi@polito.it (A.T.); silvio.vaschetto@polito.it (S.V.)
[2] Department of Industrial and Information Engineering and Economics, University of L'Aquila, 67100 L'Aquila, Italy; andrea.credo@univaq.it (A.C.); giuseppe.fabri@univaq.it (G.F.)
* Correspondence: lorenzo.perilli@polito.it

Abstract

The increasing demand for electric power in hybrid electric aircraft platforms prompts the development of multi-megawatt generators featuring high specific power, compactness and intrinsic fault tolerance. Air-core machines constitute a promising solution to overcome the magnetic saturation and mass limitations of conventional iron-core designs. This paper presents a comparative electromagnetic design study of two air-core synchronous generator topologies for aircraft applications, namely a permanent magnet machine with a Halbach array rotor and an electrically excited synchronous machine featuring a high-temperature superconducting field winding. Both the generators are designed for identical output and adopt a double three-phase stator winding to enhance safety and redundancy. The Halbach array machine is used as the reference configuration representative of a technologically mature solution, whereas the superconducting generator targets high magnetic loadings by means of the superconducting excitation, to minimize the active volume. The solutions proposed in this paper are developed in the frame of a national (Italian) research project dedicated to the study of stages of multi-megawatt fault-tolerant aircraft generators.

Keywords: hybrid electric aircraft; air-core machines; permanent magnet synchronous generator; high-temperature superconductors; multi-three-phase

Check for updates

Academic Editor: Rui Xiong

Received: 8 March 2026
Revised: 23 March 2026
Accepted: 25 March 2026
Published: 29 March 2026

Copyright: © 2026 by the authors. Licensee MDPI, Basel, Switzerland. This article is an open access article distributed under the terms and conditions of the Creative Commons Attribution (CC BY) license.

1. Introduction

The progressive electrification of air transportation systems is leading to a substantial increase in the onboard demand for electric power [1,2]. The replacement of mechanical, hydraulic and pneumatic components with electrical actuators as more efficient and more sustainable solutions, along with the introduction of hybrid electric (HE) and distributed propulsion architectures, is shifting the onboard power levels toward the multi-megawatt domain [3]. This trend imposes stringent requirements on the onboard power generation, which must deliver large output power with minimal mass and volume, while meeting severe reliability and safety constraints [4,5]. In this framework, newly conceived aircraft (A/C) generators are expected to combine a significant power-to-weight ratio with inherent fault-tolerant capabilities to ensure continuous operation under both normal and degraded conditions [6,7].

Within this context, many research activities have been prompted by public funded programs and private industrial companies to focus on the investigation of MW-range, HE

platforms for regional and wide-body A/C [8]. Turbine-driven electrical generators are envisaged as an enabling technology for air transport electrification and are regarded as a more mature alternative compared to electrochemical sources, including both batteries and fuel cells [9]. Nevertheless, to achieve the expected performance, the paradigm of electric generator design is currently shifting toward the study and use of innovative materials and configurations, which are needed to surpass the limitations of the conventional machine designs [10,11]. Among all the proposed solutions, permanent magnet (PM) synchronous generators employing Halbach array configurations and superconducting (SC) electric machines have emerged as two leading topologies for achieving high-specific-power aircraft generators.

Both Halbach array and SC electric machines can rely on reduced use of ferromagnetic materials [12,13]. With the exception of the stator yoke—which is typically included in aircraft applications also to prevent the machine flux from causing disturbances in the surrounding systems and components—air-core machine designs with unmatched power-to-weight ratios can potentially be achieved [14,15]. In addition, for high-performance applications such as the aircraft one, multiphase and multi-three-phase stator windings can result in improved overall safety and reconfiguration possibilities in case of faults [16,17]. The reduced spatial harmonic content of these winding configurations allows also mitigating the generation of the asynchronous fields and their impact on the adopted rotor technology in the different operating conditions [18]. Specifically for the multi-three-phase windings, the modularity offered by the presence of separated three-phase sets enables the convenient implementation of advanced control strategies oriented at guaranteeing satisfactory operation under faulty conditions [19].

The Halbach array generators constitute a mature technology which can eventually be integrated directly into existing aircraft platforms. The particular arrangement of PMs in this kind of machine allows reducing and ultimately removing the rotor iron yoke by guiding the magnetic flux in specific directions. Nevertheless, for high-speed operation in turbine-based onboard generation systems, mechanical robustness studies for integrity of the rotor assembly must be conducted, together with the investigation of innovative manufacturing solutions aimed at reducing the PM losses, such as PM segmentation. The use of aircraft-grade PMs with reduced sensitivity of residual magnetization to temperature variations represents the preferred choice for high-specific-power design, despite being affected by wide price oscillations and uncertain availability of the rare earth materials typically employed in the aircraft industry.

More generally, recent research on permanent-magnet synchronous machines continues to advance both their control strategies and their suitability for high-performance applications. In particular, constrained terminal-sliding-mode permanent magnet synchronous machine control strategies have recently been proposed to improve dynamic performance under speed and current limits, while recent aviation-oriented studies have further investigated MW-class high-speed PM synchronous machine topologies, including Halbach-based benchmark solutions. Although these contributions address operating scenarios different from the present work, they confirm the continuing relevance of PM-based solutions as a technologically mature reference for high-performance electrical generation systems [20–22].

Regarding SC electric machines, many recent research and prototyping activities have been dedicated to the integration of high-temperature superconductors (HTS) in electrically excited synchronous machines (EESMs) [23–25]. The high-temperature superconductors, which can exhibit superconductivity at relatively high cryogenic temperatures (greater than 35 K) by means of liquid nitrogen (LN_2), liquid neon or helium gas cooling, are suitable for the replacement of conventional Cu rotor windings of EESMs [26–28]. The near-zero DC

resistance of HTS and large current density allow achieving high magnetomotive forces in compact volumes, thus enabling air-core configurations for rare-earth-free machine designs not limited by the magnetic saturation of iron cores [29–31]. Furthermore, the possibility of regulating the no-load excitation field through the rotor current constitutes a desirable feature to strongly enhance the safety of the onboard electric systems since the EESMs can be promptly de-energized [32]. However, the realization of aircraft platforms based on SC technologies results in complex challenges related to the cryogenic cooling operation and integration with the other onboard systems [33].

In this framework, the present article focuses on the design and comparison of two topologies of air-core generators for fault-tolerant aircraft applications, based either on the Halbach array or the high-temperature superconductors. In particular, the activity is developed in the frame of the project PRIN—Italian Research Project of National Relevance 2022 "Multi-phase fault tolerant MW range generation systems for hybrid electric aircrafts" [34]. A Halbach array synchronous generator is presented as the baseline design to enable the comparison with a SC electric machine. In order to maximize the possibilities offered by the HTS, high magnetic flux densities are targeted in design stage to achieve reduced weight and size for the same output specifications. Both configurations present a double-three-phase winding and share the same stator cooling and stator electrical loading. Performance comparisons between the baseline PM machine and the proposed SC design complete the analyses developed in this article and allow highlighting advantages and disadvantages of the two topologies.

2. Halbach Array PM Generator

The Halbach array PM solution was selected as the baseline conventional machine for comparison with the SC generator since it enables the maximum achievable electromagnetic power density when PM-based machines are used. Although this topology requires the largest amount of permanent magnet material at fixed rated power, it also provides the highest air-gap flux density and torque capabilities among the non-cryogenic solutions.

Since the target application is an aerospace generator, no constraints were imposed on the PM cost. The design objective was instead focused on achieving extremely high specific power and volumetric densities.

2.1. Design Specifications

The main design requirements of the generator are reported in Table 1. It is worth noticing the extremely high rated power of 4 MVA combined with very stringent volumetric and mass constraints: the volume of the active parts must be below 40 L, while the total active mass must be below 170 kg. The DC-link voltage is imposed and equal to 1500 V, while the maximum electrical frequency at the inverter output is limited to 1500 Hz. In addition, the phase current must remain below 2000 A.

Table 1. Design specifications.

Parameter	Value
Output power	4 MVA
Rated speed	15,000 rpm
DC-link voltage	1500 V
Maximum inverter frequency	1500 Hz
Maximum phase current	<2000 A
Active parts volume	<40 L
Active mass	<170 kg
Winding type	2 × 3-phase

Several machine configurations have been investigated to meet these requirements. For clarity reasons, only the final design adopted as baseline machine is reported here, as it is used for comparison with the superconducting generator.

2.2. Multiphase High-Speed Configuration

Given the combination of rated power, DC voltage, and current constraints, the only feasible solution consists of the adoption of a multiphase stator. In particular, a double three-phase winding configuration was selected, with the two three-phase sets phase-shifted by 30 electrical degrees, in order to improve the quality of the output voltage waveform and to comply with the imposed current limit.

In the present paper, the adoption of a double three-phase stator winding should therefore be interpreted as an architecture enabling post-fault reconfiguration rather than as a complete demonstration of fault-tolerant performance. At the system specification level, the degraded operating condition considered in this design stage corresponds to the complete disconnection of one three-phase set, while the remaining healthy set is allowed to operate in overload so as to provide approximately 66% of the rated power, deemed sufficient for the supply of essential loads. A bolted short-circuit fault of a single phase was not considered at this stage. From a qualitative viewpoint, the PM generator and the HTS electrically excited machine exhibit different fault-related features: in the PM solution the excitation cannot be switched off, whereas in the electrically excited HTS machine the rotor field can be de-excited, which may provide an additional safety-related advantage.

Due to the extremely small available volume, a high-speed solution was mandatory. However, due to the maximum allowable electrical frequency, the rated speed was limited to 15,000 rpm, leading to the selection of a 10-pole rotor.

2.3. Slotless Stator and Thermal Constraints

The severe mass constraint led to the adoption of a slotless stator combined with a stator back-iron ring to confine the high magnetic flux.

This choice is also driven by the very high air-gap flux density required to meet the torque demand. Any conventional magnetic material (including high-cobalt iron–cobalt alloys) resulted in unacceptable magnetic saturation. Furthermore, stator teeth would drastically reduce the available slot area, limiting conductor cross-sections and making direct cooling solutions impractical. For these reasons, the slotless topology was selected.

Nevertheless, direct oil cooling of the conductors is still required, with flow rates exceeding 400 L/min, to sustain current densities of approximately 15 A_{rms}/mm^2.

2.4. Winding Data

The main winding parameters are reported in Tables 2 and 3.

Table 2. General winding data.

Parameter	Value
Equivalent slots	180
Number of phases	6
Winding type	Lap
Phase distribution	$N\times$ 3-phase
Path type	Central
Turns per coil	5
Coil pitch (throw)	18 slots
Parallel paths	10
Winding layers	2
Offset	42
Multiplex offset	3

Table 3. Wire and slot filling parameters.

Parameter	Value
Coil style	Stranded
Divider type	Overlapping
Winding definition	Wire size
Wire type	Diameter input
Overall wire diameter	0.585 mm
Copper diameter	0.55 mm
Number of strands per conductor	40
Number of wire sizes	1
Conductors per slot	400
Conductors per slot (drawn)	400
Wire slot fill (winding area)	0.3754
Wire slot fill (slot area)	0.3730
Copper slot fill (slot area)	0.3297
Heavy build slot fill	0.4779
End-winding fill factor	0.4842
Liner thickness	0.25 mm
Conductor separation	0.10 mm
Copper depth	100%
End-winding mean length turn (MLT)	418.73 mm
Potting goodness (end-winding)	1

2.5. Rotor and Halbach Array Geometry

The Halbach configuration combined with the slotless stator allows full compliance with the application requirements. The permanent magnets have a thickness of 27 mm and are segmented into four magnets per pole in a sinusoidal Halbach array in order to maximize the extractable torque within the selected rotor volume.

The rotor outer diameter is 354 mm, while the magnetic air-gap is 3 mm, required to accommodate the composite fiber retaining sleeve and the adhesive layer needed to guarantee mechanical integrity at high speed. The peripheral rotor speed places the machine in the category of high-speed electrical machines. The fiber sleeve was selected to minimize additional losses and reduce its impact on the magnetic air-gap, while ensuring exceptional mechanical performance.

The finite element model of the Halbach PM generator is reported in Figure 1; one pole pair is represented and the different colors are used to distinguish the stator phases, for which a distributed winding is adopted.

$$v = \omega r = 2\pi \cdot \frac{15,000}{60} \cdot 0.177 \approx 278 \text{ m/s}. \quad (1)$$

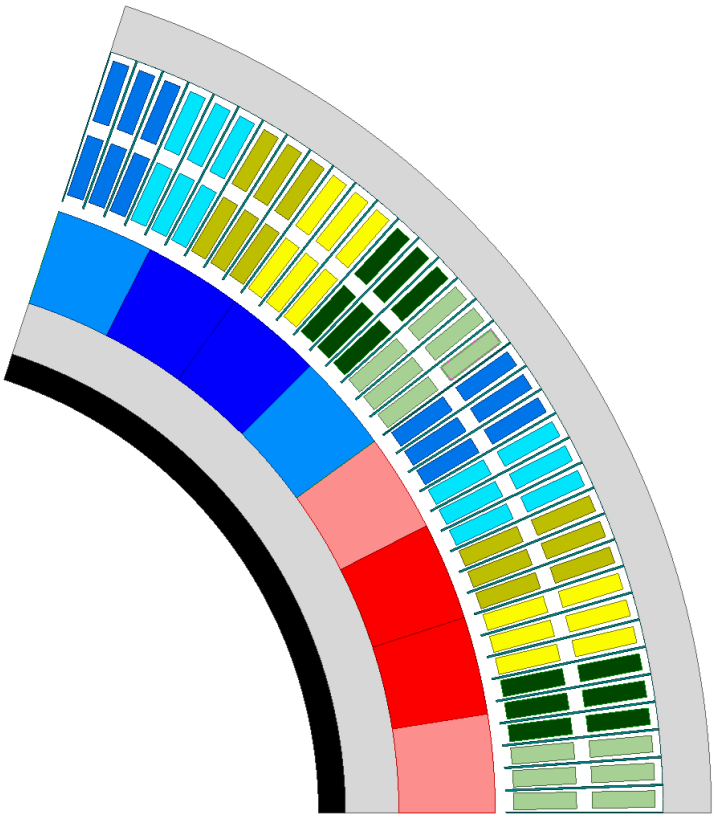


Figure 1. Finite element model of a pole pair of the Halbach PM synchronous generator.

3. HTS Electrically Excited Synchronous Machine

The proposed design of superconducting EESM presents copper stator winding and rotor winding made of HTS. The SC machine features the same configuration of stator winding as the Halbach array baseline design discussed previously, i.e., a double-three-phase winding for enhanced safety and fault tolerance. Additionally, the HTS on the rotor firstly makes it possible to regulate or promptly remove the excitation field and, secondly, to achieve large induction distributions for reduced weight and size.

The SC machine has been sized by means of analytical equations, whose output has been later verified and tuned by means of finite element analyses. In this regard, the output power of the machine can be expressed as:

$$S = \frac{\pi^2}{\sqrt{2}} k_{w,1} \hat{B}_{s,1} A_s D^2 L n_s \tag{2}$$

In which $k_{w,1}$ is armature winding factor for the fundamental harmonic; $\hat{B}_{s,1}$ and A_s are the flux density (magnetic loading) and the linear current density (electric loading), respectively, at the mean diameter of the armature winding; D is mean diameter of the armature winding; L is the machine active length; n_s is the mechanical speed of the rotor in revolution per second [35]. It should be noted that (2) remains formally the same for both conventional, iron-core machines and air-core machines. In this regard, for conventional generators, the magnetic and electric loadings are referred to the air gap of the machine, and the magnetic loading specifically constitutes a measure of the flux density in the iron teeth. Conversely, for air-core configurations, the magnetic fields can change significantly between the internal and external diameters of the armature winding and the mean value can, thus, be considered in the sizing stage [36]. The D and L are therefore determined from

(2) by introducing the form factor, referred to the mean diameter of the armature winding and defined as:

$$\chi = \frac{L}{D} \tag{3}$$

In order to enable the comparison with the PM Halbach array baseline machine, an identical value of electric loading (200 kA/m) has been chosen for the SC machine design, as well as the same surface current density of the stator conductors. However, to achieve the reduced use of active materials and exploit the possibilities offered by the HTS, a target value of 2.5 T has been selected for the magnetic loading [37]. These design choices have led to the machine D and L listed in Table 4. Additionally, the SC machine has been designed to satisfy the target performance with an external diameter of the stator iron shield which is not larger than that of the baseline PM machine.

Successively, the number of turns N_1 in series per phase of the armature winding can be determined from the no-load phase voltage E_0 as:

$$N_1 = \frac{E_0}{\sqrt{2}\pi k_{w,1}\hat{\Phi}_1 f} \tag{4}$$

In which f is the electrical frequency. The flux per pole $\hat{\Phi}_1$ is related to the considered magnetic loading by means of (5), with p being the number of pole pairs.

$$\hat{\Phi}_1 = \frac{\hat{B}_{s,1} DL}{p} \tag{5}$$

In order to complete the definition of the stator winding, the number n_c of armature conductors per 'equivalent' slot in the air gap is determined as follows:

$$n_c = \frac{N_1}{qp(1/a)} \tag{6}$$

where q is the number of equivalent slots per pole and per phase since the stator winding is placed in the air gap and there are no magnetic teeth, and a is the number of stator parallel current paths [37]. The corresponding cross-section of the copper conductors can be obtained from the nominal current I_n and the surface current density J_s, as [38,39]:

$$S_{Cu} = \frac{I_n}{aJ_s} \tag{7}$$

Finally, the slot surface S_{slot} can be determined by introducing the filling factor k_{fill}:

$$S_{slot} = \frac{S_{Cu} n_c}{k_{fill}} \tag{8}$$

in which the k_{fill} adopted here takes into account also the supporting structure for the air gap winding, considered as a fraction of the stator slot pitch [36].

In the no-load condition, the flux density $\hat{B}_{s,1}$ in (4) is generated solely by the current in the SC field winding. An estimation of the corresponding value can be obtained through analytical expressions, using the so-called '*current-sheet*' formulation of air-core machines. In this regard, the machine is considered as a combination of concentric annular domains, and the magnetomotive forces are considered as concentrated at the mean radius of the windings (stator and rotor). In the literature, different formulations can be found to compute $\hat{B}_{s,1}$ [40,41]. In this case, the formulation proposed in [42] has been considered to obtain a fast sizing of the machine with reduced computational effort. However, the analytical results have been later verified and tuned by means of finite element simulations. In order

to achieve the target value of 2.5 T for the flux density fundamental, a 4-pole configuration has been chosen for the SC machine [43].

Table 4. Main data of the superconducting EESM.

Parameter	Symbol	Value
Magnetic loading	$\hat{B}_{s,1}$	2.5 T
Electric loading	A_s	200 kA/m
Fundamental winding factor	$k_{w,1}$	0.9598
Stator internal diameter	n.d.	0.2261 m
Armature winding diameter	D	0.2606 m
Stator yoke internal diameter	D_{sy}	0.2951 m
Stator yoke external diameter	n.d.	0.4579 m
Active length	L	0.0704 m
Form factor	χ	0.27
No-load phase voltage, rms	E_0	570 V
Mechanical speed	n_s	250 rps
Stator turns in series per phase	N_1	12
Pole pairs	p	2
Slots per pole per phase	q	3
Conductors per slot	n_c	160
Parallel current paths	a	80
Stator current, rms	I_n	1166 A
Surface current density	J_s	14 A/mm^2
Conductor area	S_{Cu}	1.042 mm^2
Filling factor	k_{fill}	0.425
Slot area	S_{slot}	392.1 mm^2

While the stator yoke diameter is affected by the pole number selection, the saturation induction of the ferromagnetic material and also limited by the design constraints, the mean rotor winding diameter is strongly influenced by the radial thickness of the cryostat for maintaining the HTS at cryogenic temperature. Indeed, lower induction values are obtained when the rotor winding is placed at a considerable distance from the stator due to the presence of the cryogenic vessel. In the proposed machine design, liquid nitrogen cooling (77 K) is adopted for REBCO tapes (whose specification can be found in Table 5) and a cryostat thickness of 15 mm is assumed [44]. Specifically for the tapes, the rated current has been limited to approximately 65% of the critical current in self-field at 77 K to avoid quenching when the HTS are exposed to the magnetic fields of the electric machine. Within this framework, the accurate simulation of the HTS performance would require the implementation of specific formulations for finite element analyses, such as the **T-** or **H-**formulations [45]. However, this approach could lead to significant computational times, and a constant current density is considered here for the tapes to analyze the macroscopic effect on the power density, thanks to the margin adopted for the critical current [46,47].

Furthermore, the proposed HTS winding adopts a no-insulation (NI) configuration and, therefore, quench protection is enhanced by intrinsic current redistribution, while can also be achieved by means of additional external active protection measures. Specifically, differently from fully insulated coils, the NI winding provides an inherent turn-to-turn current bypass path. When a local section of HTS tape transitions to the normal state, part of the transport current can transfer to the adjacent turns through the contact resistance, which suppresses the local hot-spot temperature rise and delays thermal runaway. This intrinsic current-sharing effect improves quench tolerance compared with conventional insulated windings. Additionally, the operating HTS current is limited with respect to the

datasheet value corresponding to the self-field case, thus mitigating the risk of potential damage from external magnetic fields and associated critical current reduction. All these considerations soften the requirements for the development of active protection measures.

With these specifications, the analytic design has been completed and verified through finite element simulations, verifying that the machine achieves the target performance and that the minimal bending radius of the HTS tapes is not surpassed. In addition to that, the distance between the outer diameter of the rotor cryostat and the internal diameter of the stator winding (which can be assumed to be a physical air gap between rotor and stator) has been kept at 3 mm, as in the PM machine. The finite element model of the SC generator is reported in Figure 2. The HTS tapes have been positioned as a racetrack-type, double-pancake coil and additional space has been envisaged for support and casing [47]. One pole pair is represented in Figure 2, and the different colors are used to distinguish the stator phases, for which a distributed winding is adopted. Moreover, the mean armature winding diameter can be also observed.

Table 5. Main data of the HTS field winding.

Parameter	Value
Rotor current	530 A
Rotor turns per pole	1150
Mean rotor winding diameter	0.1481 m
Cryostat thickness	0.0150 m
Cryostat external diameter	0.2201 m
Tape manufacturer	SuNAM
Tape technology	REBCO
Tape width	12 mm
Tape thickness	100 µm
Critical current (77 K, self-field)	800 A
Utilization factor	$\sim$ 65%
Cryogenic coolant	LN_2
Coolant temperature	77 K

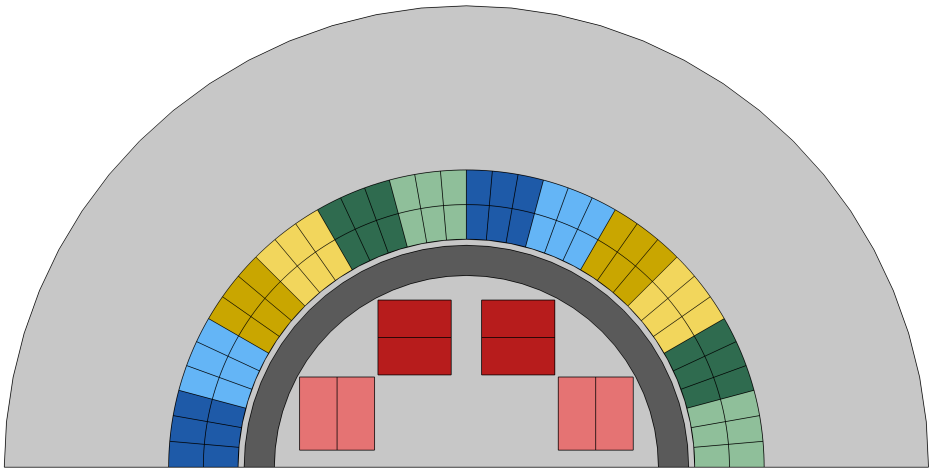


Figure 2. Finite element model of a pole pair of the SC electrically excited synchronous generator.

Experimental Assessment of Rotor Resistance Variation

In order to validate the assumptions formulated in the electromagnetic design stage regarding safety margins for the operation of HTS rotor windings, an experimental setup has been implemented to assess the voltage drop and quenching of HTS tapes. The tests have focused on the impact of the magnetic fields generated by other machine windings,

i.e., the stator windings, on the steady-state voltage drop and on the corresponding DC resistance of the rotor superconductors.

For this purpose, a reduced-scale mock-up has been realized using the stator of a conventional 550 W, 4-pole induction machine and an isotropic rotor iron core. The iron core has been retained to reduce HTS material usage by increasing the magnetic permeability compared to air-core machines, while providing mechanical support for the HTS tapes. The EESM mock-up has been tested in a liquid nitrogen bath (77 K) with locked-rotor, as shown in Figure 3. Both rotor HTS field winding and stator copper windings have been supplied in DC to create stationary fields. Different configurations have been analyzed by permuting the stator phases, which have allowed the resulting stator current vector to be oriented in different positions in the *dq* reference frame (*d*-axis corresponding to the magnetic axis of the rotor winding). The results of the laboratory tests are presented in Figure 4. In addition, the simulation results are also reported, which have been obtained by implementing the **T-A** formulation in a commercial finite element software.

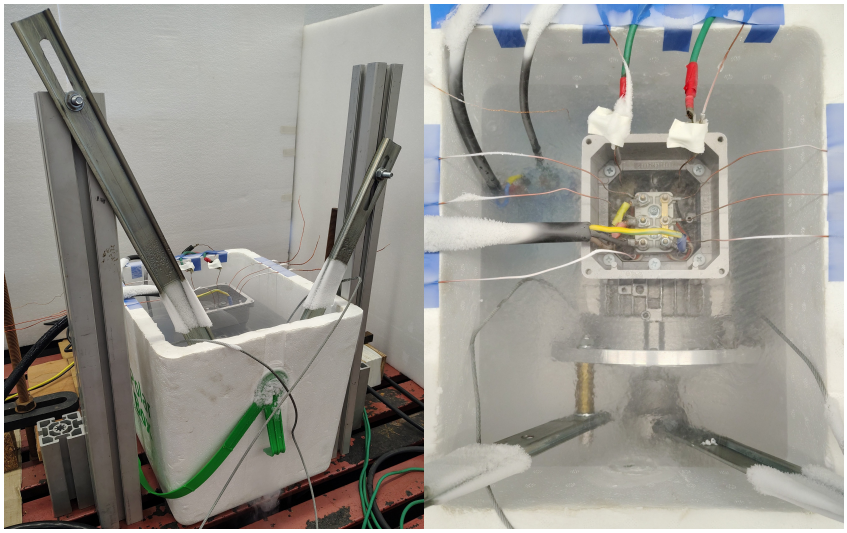


Figure 3. Experimental setup for the assessment of performance for HTS tapes.

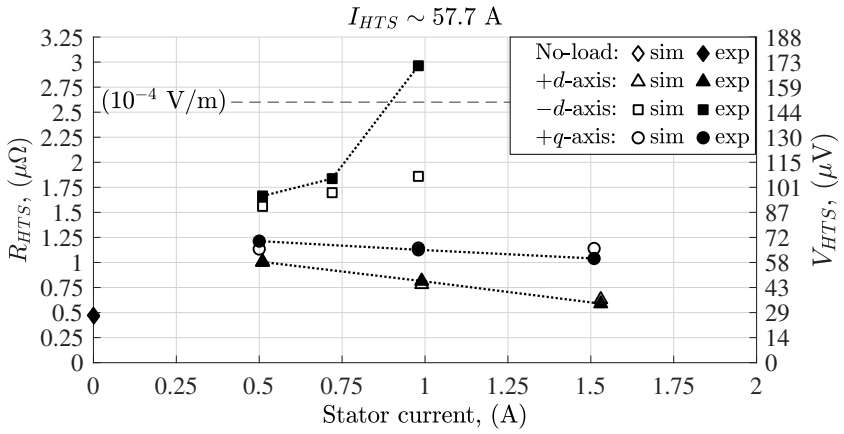


Figure 4. Results of the experimental tests and comparison with the simulation model.

As it can be observed from the variations of resistance and voltage drop, the effect of the stator current consists of altering the induction distribution in the region where the superconductors are positioned, in a way that the HTS performance is affected significantly. Indeed, magnetic fields change the conduction characteristic of superconductors, leading to different values of critical current and of corresponding voltage drop. In this particular case, the *d*-axis current has the largest impact, decreasing (positive case) or increasing (negative

case) the leakage flux lines hitting the superconductors. Conversely, the resistance and voltage drop of the HTS remain almost constant when stator q-axis current is applied due to the isotropic iron core configuration. In one specific point (1 A and negative d-axis current) quench has been observed experimentally, even though the operating current of the HTS tapes corresponds to approximately 70% of the self-field value. For the air-core EESM proposed in the paper, 65% has been considered, and it must also be noticed that stator current vectors oriented in negative d-axis do not constitute machine operating points (zero torque). Regarding the simulation results, good agreement with the measured data is observed for the finite element model. However, the introduction of the temperature dependency may be necessary to detect quenching by analyzing the local HTS losses.

4. Comparison Results

To ensure a fair comparison of the two machines, which were originally designed using different numerical tools, the same commercial software platform has been adopted to derive the efficiency and performance maps presented in the following. In this study, *Ansys Motor-CAD* was selected because it enables convenient and consistent characterization of both machine typologies. The simulations were performed to assess the performance of the two machines in terms of efficiency, losses, and compliance with the required operating point (4 MVA at 15,000 rpm). In addition, weight and size comparisons are first presented.

The final Halbach-array design reported in this paper was obtained through a single-objective optimization process aimed at maximizing the efficiency at the design operating point. The optimization was constrained by the imposed volumetric envelope, the required torque-speed performance, the phase to phase voltage compatibility with the selected DC bus, and the maximum allowable steady-state temperatures in both the stator conductors and the permanent magnets. These constraints, except for the PM one, have been adopted also for the HTS machine design.

The design variables considered in the optimization of the Halbach-array machine were the PM height, the stator inner diameter, and the stator back-iron thickness. After the numerical optimization, a further refinement stage was carried out in order to obtain dimensions compatible with a possible manufacturing process. Owing to the limited number of optimization variables and to the preliminary analytical sizing used to restrict the search space, the optimization converged in approximately 300 iterations. On the other hand, for the superconducting EESM, the optimization has been oriented toward minimizing the volume of SC material by adopting a different number of pole pairs compared to the PM case, active length and stator inner diameter. Iterative analytical computations provided a starting point for finite element simulations, which have been used to refine the proposed machine design and ensure possible practical implementation and manufacturing of the HTS coils.

To reduce the computational burden, only periodic portions of the two machines were simulated by exploiting the geometrical and electromagnetic symmetries of the models. All the reported results were obtained from transient electromagnetic analyses, rather than multi-static simulations, in order to improve the accuracy of the loss estimation.

For the full finite element analyses, a refined discretization was adopted in the air-gap region by imposing 1440 points along the air gap, with additional local refinement in the magnet and conductor regions, which are the most critical areas for AC-loss estimation. A coarser mesh was then employed for the generation of the efficiency and loss maps, while maintaining the same discretization logic. In all cases, the maximum element size was limited to 0.5 mm, and the mesh was automatically further refined whenever this threshold was not satisfied.

This methodology provides reliable numerical indicators for comparative purposes. Although commercial software does not guarantee absolute accuracy, it is widely validated and suitable for benchmarking studies. All the required input data were implemented in the simulations, and a relatively fine mesh was adopted to achieve a complete machine mapping within acceptable computational time. For all the comparison plots, the reported difference is defined as:

$$\Delta(\cdot) = (\cdot)_{\mathrm{SC}} - (\cdot)_{\mathrm{Halbach}} \tag{9}$$

Regarding the power electronics converters for the electric machine output, the similar voltage and current levels of the stator windings between PM and HTS machines allow using comparable power electronics components for the two case studies, thus enabling the performance comparison. Additionally, for the HTS machine in the finite element environment, an ideal current source for the SC rotor winding has been considered, and the impact of the current ripple on the performance of the superconductors has been disregarded.

4.1. Power Density Comparison

For the weight and power density calculation of the two machines, the total weight includes stator copper insulation and also considers the empty spaces in the stator winding, as well as their support for air-gap placement. Specifically for the superconducting EESM, the weight of the cryogenic vessel has been included. The HTS coils support structures and frames are not explicitly modeled at this stage, as their design is strongly dependent on detailed mechanical implementation and manufacturing constraints, which are beyond the scope of this study and would introduce uncertainty in the estimation [48]. Notably, the impact of weight of the cryogenic system of the aircraft is also not taken into account [49]. Indeed, the cryogenic system (e.g., liquid nitrogen storage, distribution, and auxiliary power) has not been included because the intended application assumes aircraft-level integration of a shared cryogenic infrastructure [50]. In such configuration, the cryogenic system weight cannot be uniquely attributed to the SC machine, and assigning its full mass to the machine would not be representative.

For the volume, the external diameter is the same as the PM machine, but the length is approximately 30%. The comparison is reported in Table 6.

Table 6. Comparison of weight and power density.

Parameter	**Value**	
Iron density	7700 kg/m^3	
Copper density	8960 kg/m^3	
HTS density	8300 kg/m^3	
PM density	7500 kg/m^3	
	Weights	
Parameter	**SC Machine**	**Halbach Machine**
Iron weight	52.37 kg	51.43 kg
Copper weight	15.12 kg	64.09 kg
HTS + cryostat	27.09 kg	–
PM weight	–	43.69 kg
Total weight	94.58 kg	159.21 kg
Volume	0.0116 m^3	0.0372 m^3
	Densities	
Parameter	**SC Machine**	**Halbach Machine**
Power-to-weight	42.29 kVA/kg	25.12 kVA/kg
Power-to-volume	344.8 MVA/m^3	107.5 MVA/m^3

4.2. Efficiency Maps and Efficiency Difference Neglecting AC Losses

In the following subsections, the main performance parameters of the machines are evaluated under two operating conditions: neglecting AC losses and accounting for them. In the first case, a maximum stator current control strategy is adopted, whereas in the second case, a maximum efficiency control strategy is implemented. In particular, when AC losses are included, the control optimization is performed differently for the two solutions. For the Halbach PM machine, different stator current control angles were investigated and, at each operating point, the angle yielding the highest efficiency, i.e., the minimum total losses at the required torque, was selected. For the HTS electrically excited synchronous machine, the optimization was carried out jointly on the stator current control angle and on the rotor field current in order to identify the combination that minimized the total losses. This approach is required due to the significant contribution of AC losses, which would otherwise lead to unsatisfactory efficiency levels over a wide portion of the operating range. The adoption of different control strategies affects the distribution of the individual loss components when AC losses are neglected or included. Figures 5 and 6 report the efficiency maps of the Halbach array PM machine and the HTS electrically excited synchronous machine neglecting the AC losses, respectively, while Figure 7 shows the corresponding efficiency difference $\Delta\eta$. Both machines exhibit very high peak efficiencies; however, the Halbach solution reaches a slightly higher maximum value (99.63%) compared to the HTS machine (99.51%). Despite this, the HTS machine presents a wider high-efficiency region, resulting in superior efficiency over a large portion of the operating map. Nevertheless, operation with rated rotor current has been simulated for the superconducting EESM and further increase in efficiency is expected if a maximum efficiency control strategy with variable rotor current is implemented, which is anyway beyond the scope of the work.

In particular, the HTS generator provides higher efficiency around the most relevant operating condition for the target application, i.e., the rated point at 15,000 rpm and 4 MVA. The regions where the Halbach machine performs better are mainly located at medium-to-low torque and medium-to-high speed, as clearly highlighted by the efficiency difference map in Figure 7, where negative values indicate a local advantage of the Halbach solution.

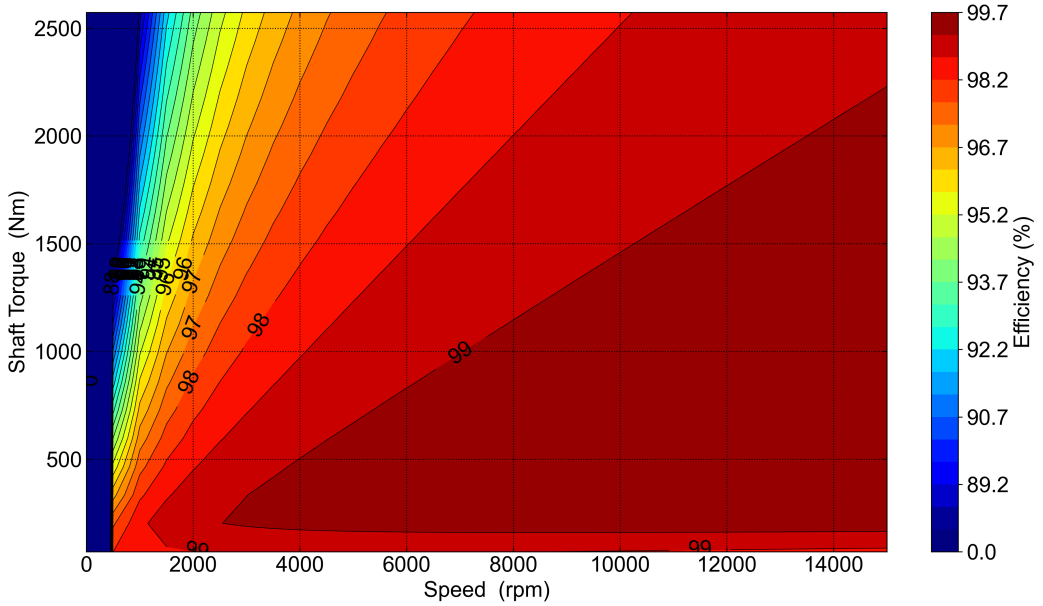


Figure 5. Efficiency map of the Halbach PM machine.

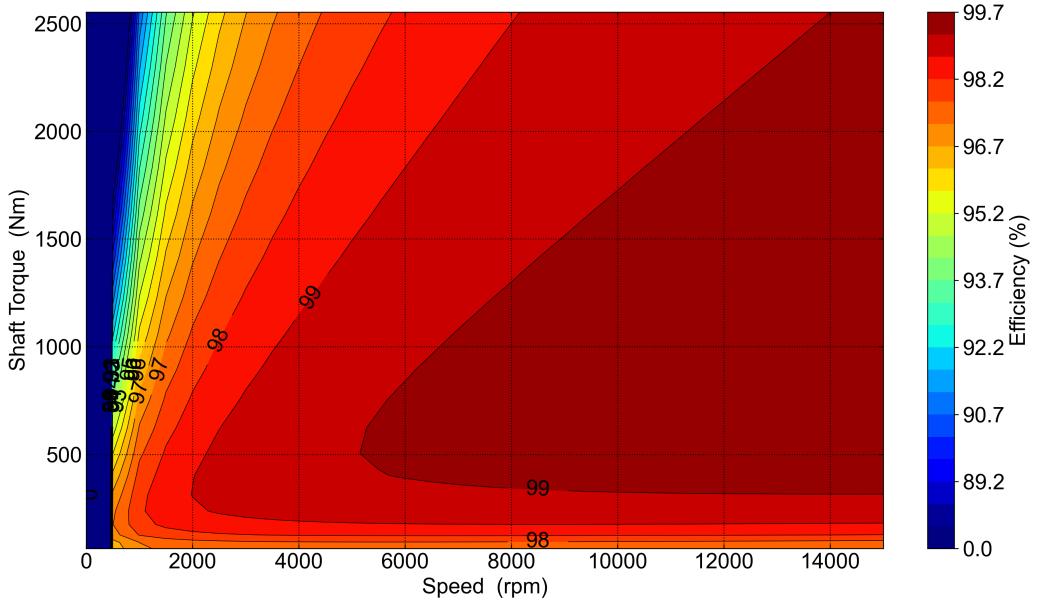


Figure 6. Efficiency map of the HTS electrically excited synchronous machine.

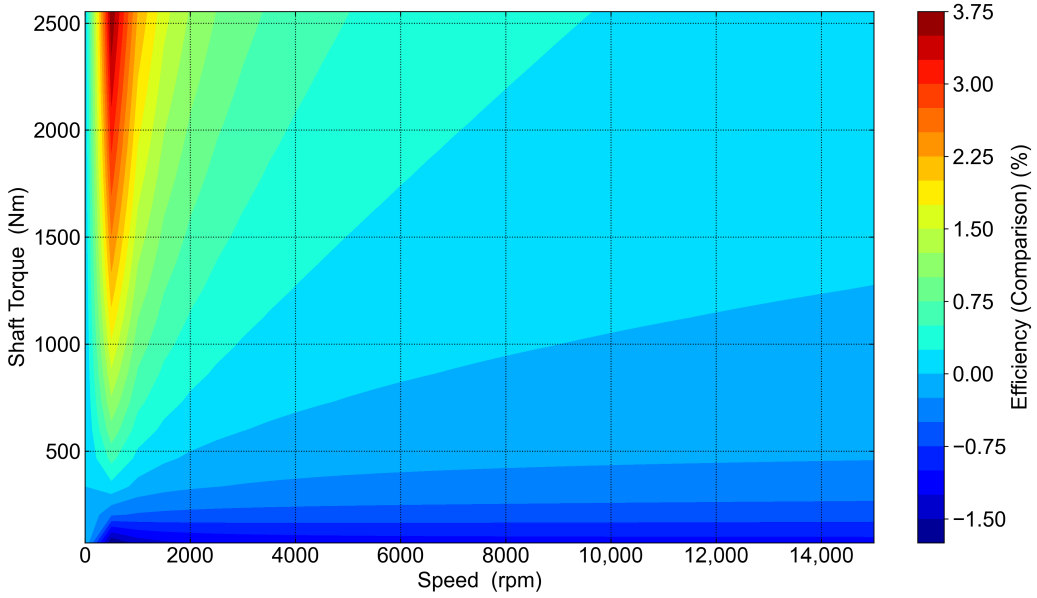


Figure 7. Efficiency difference map, $\Delta\eta = \eta_{SC} - \eta_{Halbach}$.

4.3. Total Loss Maps and Total Loss Difference Neglecting AC Losses

Although both machines achieve extremely high efficiency, it is still relevant to analyze the absolute loss levels in the operating envelope. Figures 8 and 9 show the total losses for the Halbach and HTS machines neglecting the AC losses, respectively, while Figure 10 reports the difference $\Delta P_{loss,tot}$.

The maximum total losses occur in the Halbach machine, reaching values in the order of 37 kW at high torque and high speed. In contrast, the HTS machine exhibits a lower maximum total loss, approximately 30 kW, under comparable operating conditions. Consistently with the efficiency comparison, the total loss difference map highlights operating regions where the Halbach solution becomes competitive, again mainly at medium-to-low torque and medium-to-high speed, while the HTS machine shows a clear advantage in the high-power region and around the rated operating point.

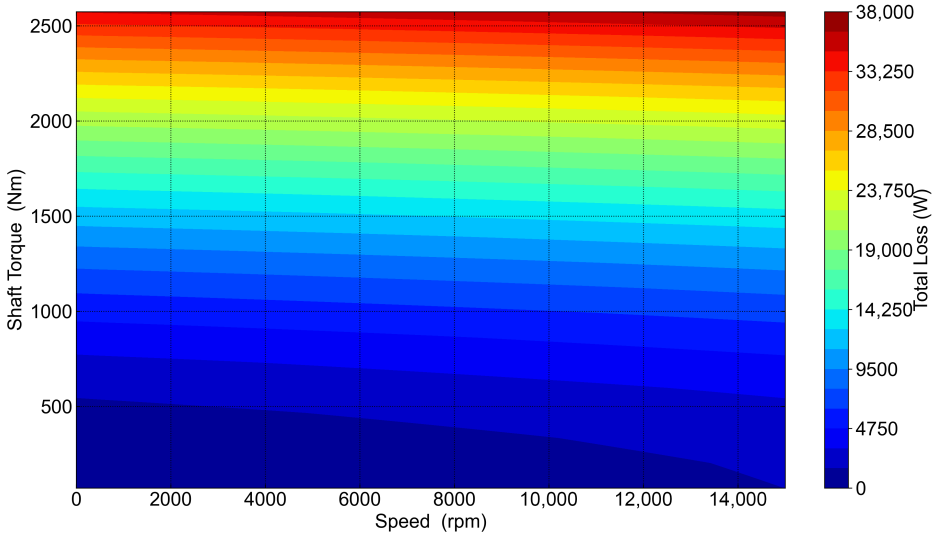


Figure 8. Total loss map of the Halbach PM machine.

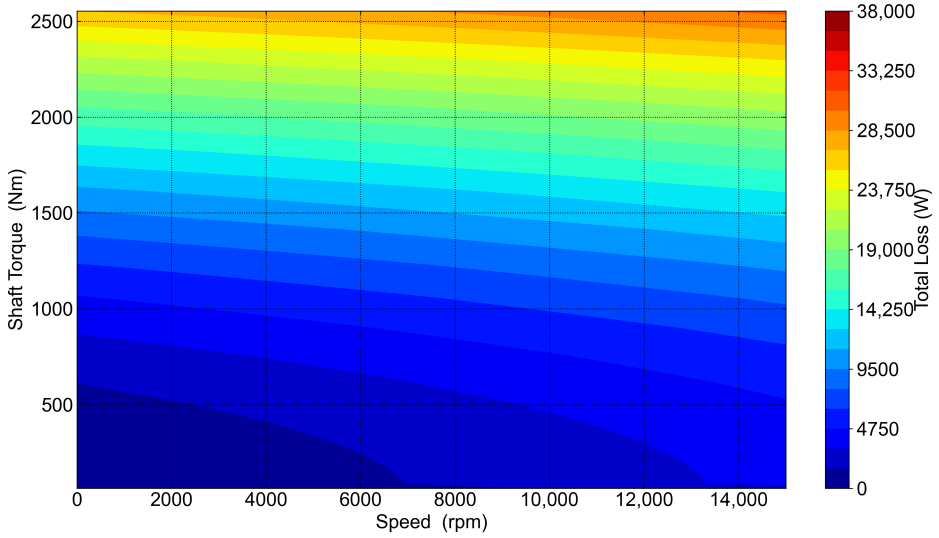


Figure 9. Total loss map of the HTS electrically excited synchronous machine.

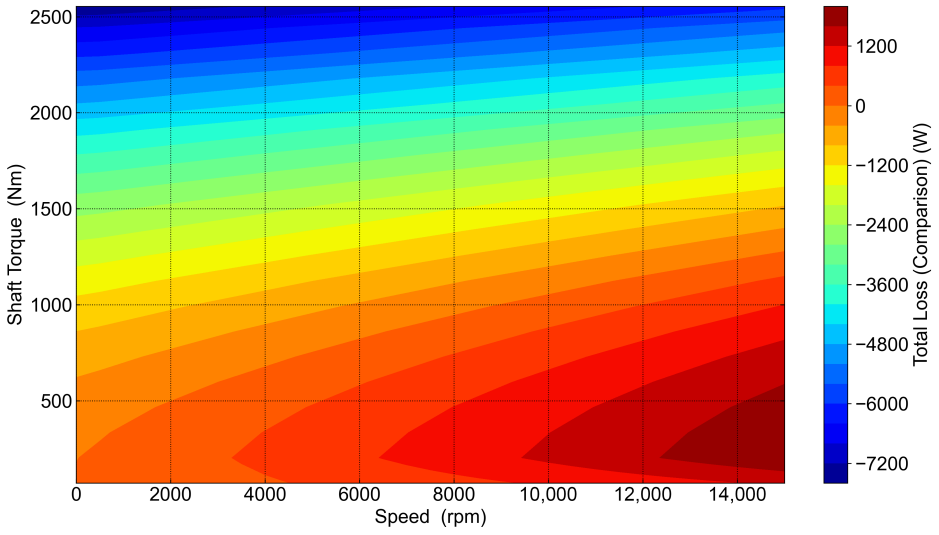


Figure 10. Total loss difference map, $\Delta P_{\text{loss,tot}} = P_{\text{loss,tot,SC}} - P_{\text{loss,tot,Halbach}}$.

4.4. DC Stator Copper (Joule) Losses Neglecting AC Losses

To provide additional insight, the two main loss components are analyzed separately, the DC stator copper losses and the iron losses. Figures 11 and 12 report the stator copper losses for the Halbach and HTS machines, respectively, while Figure 13 shows the copper loss difference.

The stator copper losses are consistently higher in the Halbach machine. This behavior can be explained by the fact that, despite the same current density being imposed, the Halbach solution features a larger active length and therefore a higher phase resistance. Moreover, the two machines exhibit similar torque-per-current characteristics, implying comparable current levels at corresponding operating points and reinforcing that the observed difference is primarily attributable to the different winding resistance rather than to substantially different current demand.

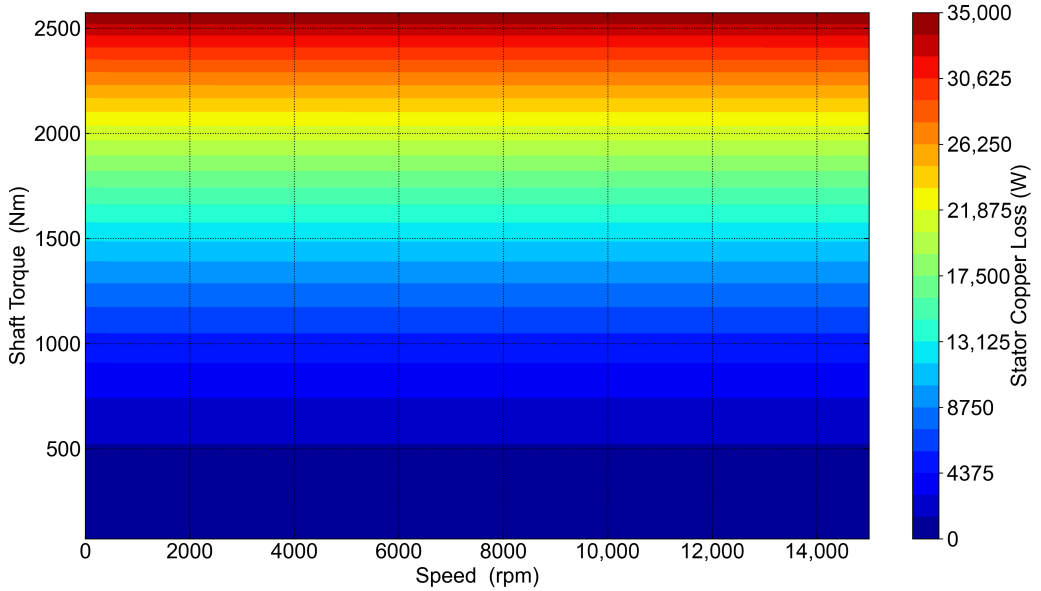


Figure 11. DC Stator copper (Joule) loss map of the Halbach PM machine.

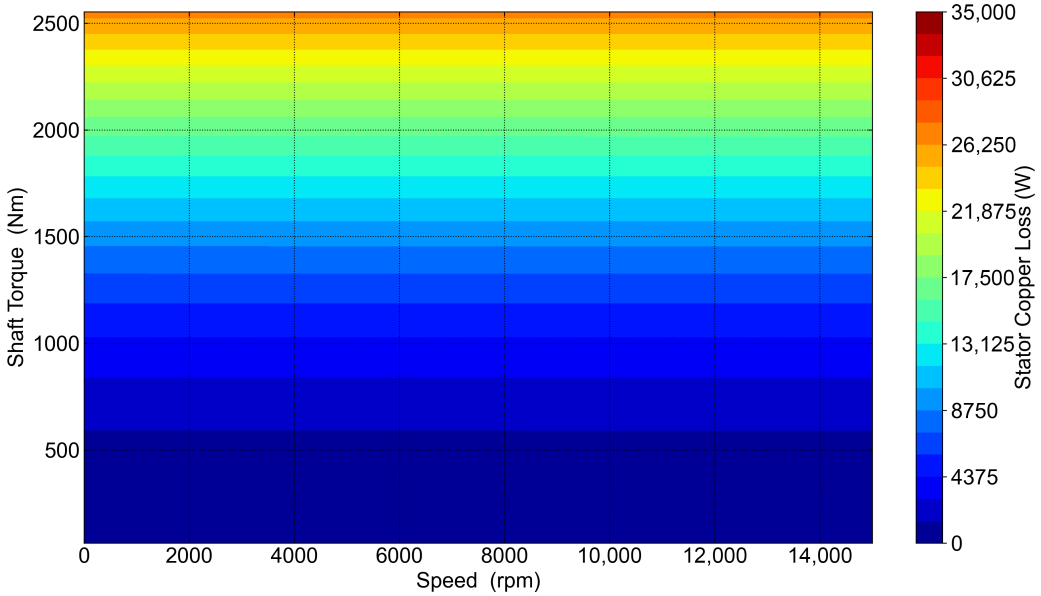


Figure 12. DC Stator copper (Joule) loss map of the HTS electrically excited synchronous machine.

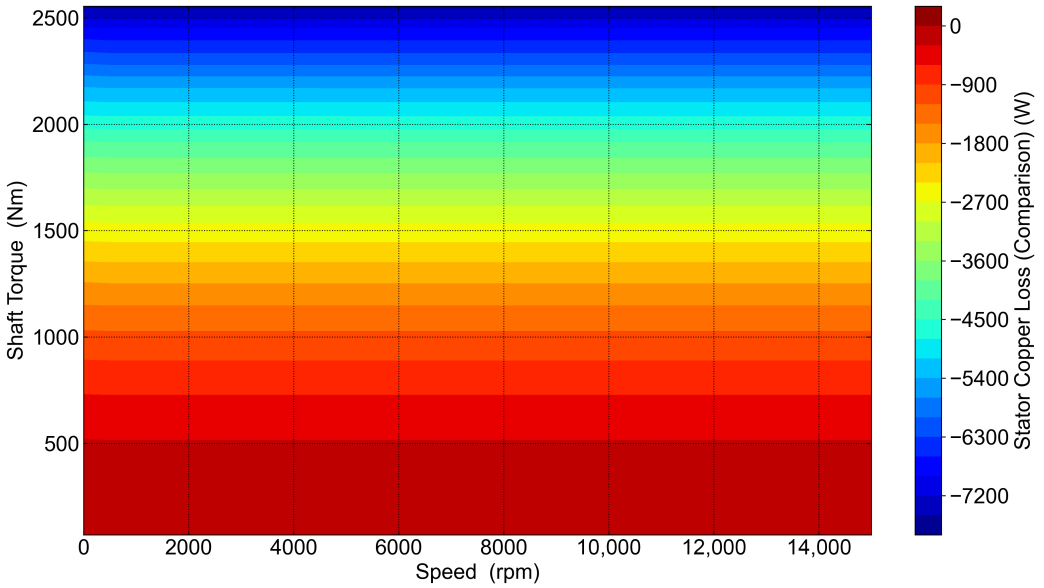


Figure 13. DC Copper loss difference map, $\Delta P_{\mathrm{Cu,DC}} = P_{\mathrm{Cu,DC,SC}} - P_{\mathrm{Cu,DC,Halbach}}$.

4.5. Iron Losses

Finally, the iron loss maps are reported in Figures 14 and 15, together with the difference map in Figure 16. The HTS machine was designed to achieve a significantly higher air-gap flux density through the very high rotor excitation currents enabled by the SC technology. As a consequence, the magnetic flux density within the ferromagnetic shield/yoke is higher than in the Halbach machine. This effect leads to increased core losses for the HTS solution, even though the electrical frequency is lower due to the reduced pole number (both machines operate at the same mechanical speed, but the HTS design employs fewer poles).

This outcome is also consistent with the geometrical design choices: the stator ferromagnetic ring (iron shield) of the HTS machine is visibly more substantial than that of the permanent magnet machine, reflecting the need to manage the higher magnetic loading.

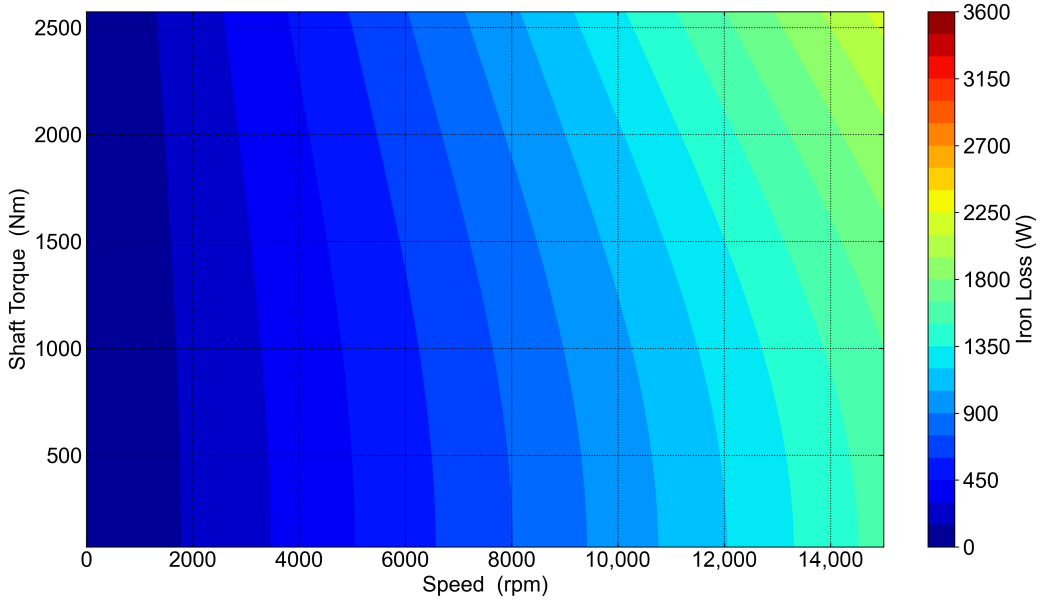


Figure 14. Iron (core) loss map of the Halbach PM machine.

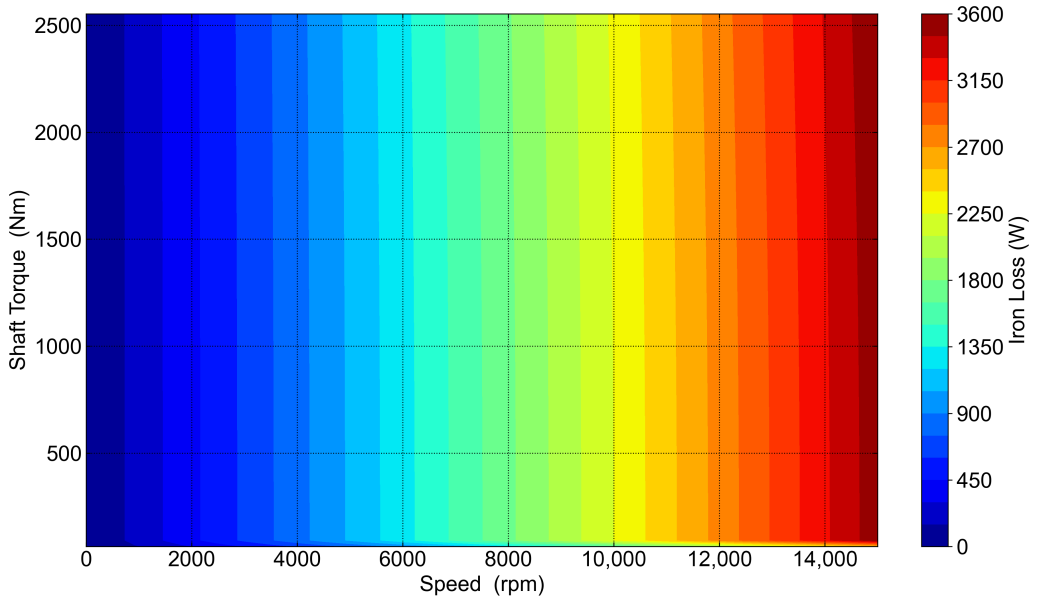


Figure 15. Iron (core) loss map of the HTS electrically excited synchronous machine.

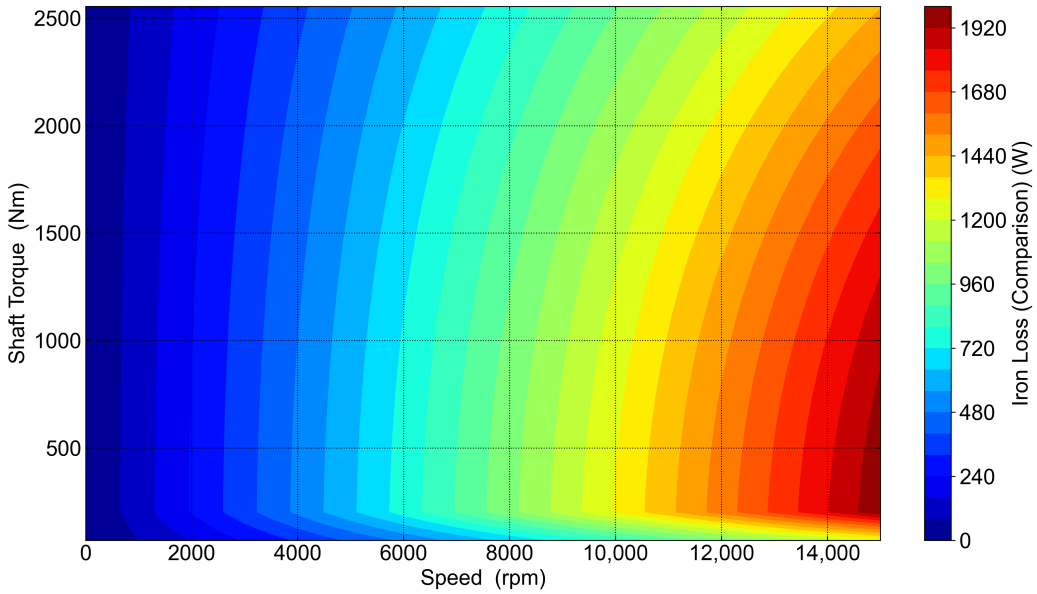


Figure 16. Core loss difference map, $\Delta P_{\text{core}} = P_{\text{core,SC}} - P_{\text{core,Halbach}}$.

4.6. Efficiency Maps and Efficiency Difference Including AC Losses

When AC losses are included, the control strategy shifts to different operating points for the HTS electrically excited synchronous machine. In particular, the control adopts a reduced rotor current in order to decrease the air-gap flux density. This adjustment is required to mitigate the proximity effect in the stator windings and, consequently, to limit the AC losses.

Figures 17 and 18 show the efficiency maps of the Halbach array PM machine and the HTS electrically excited synchronous machine with AC losses included, respectively, while Figure 19 reports the corresponding efficiency difference, $\Delta\eta$. When AC losses are considered, the efficiency of both machines is significantly reduced due to their substantial contribution. Under these conditions, the Halbach PM machine achieves the highest efficiency, reaching 97.68% in the maximum torque and maximum speed region. While the HTS electrically excited synchronous machine exhibits a peak efficiency of 97.1% in the

medium-torque, medium-speed region. Compared with the previous analysis neglecting AC losses, the overall behavior of the machines changes, highlighting the strong impact of AC losses on efficiency evaluation, particularly for the HTS electrically excited synchronous machine, which operates at higher air-gap flux density.

Thanks to the possibility of reducing the rotor current in the low-torque region, the HTS machine achieves higher efficiency under those operating conditions, as shown in Figure 19. In contrast, the Halbach PM machine provides higher efficiency in the high-speed, high-torque region, especially at the rated operating point (15,000 rpm, 4 MVA), which represents the most relevant condition for the target application.

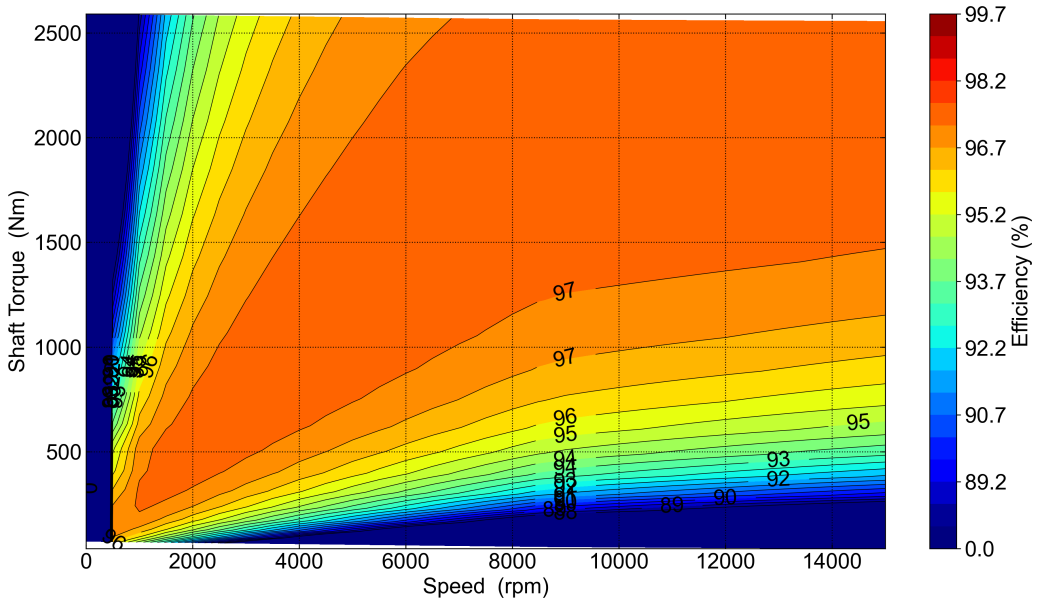


Figure 17. Efficiency map of the Halbach PM machine including AC losses.

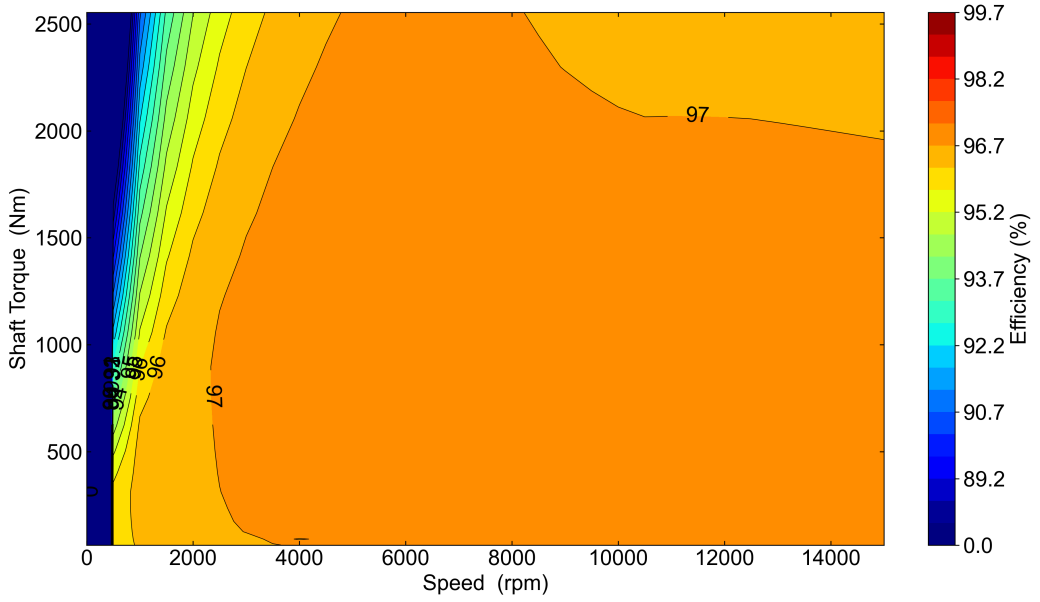


Figure 18. Efficiency map of the HTS electrically excited synchronous machine including AC losses.

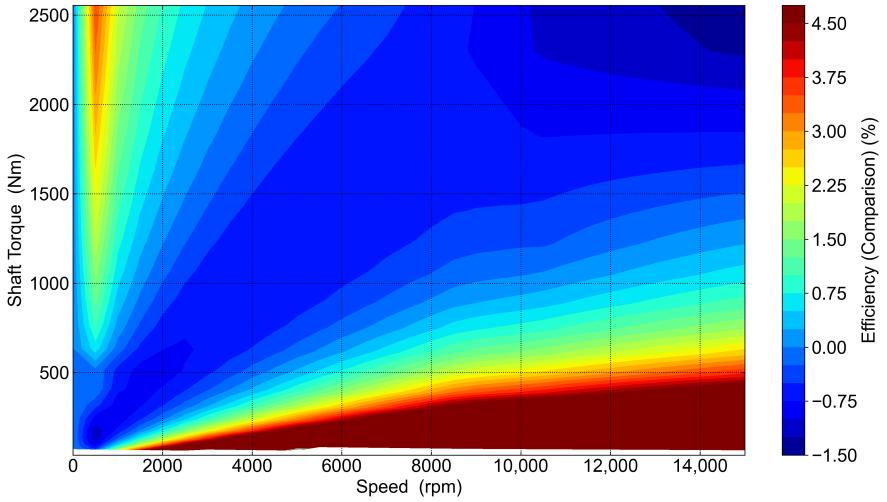


Figure 19. Efficiency difference map, $\Delta\eta = \eta_{SC} - \eta_{Halbach}$ including AC losses.

4.7. Total Loss Maps and Total Loss Difference Including AC Losses

Although both machines maintain a good efficiency when AC losses are included, it remains essential to analyze the absolute loss levels over the operating envelope. Figures 20 and 21 present the total losses of the Halbach PM machine and the HTS electrically excited synchronous machine, respectively, with AC losses accounted for, while Figure 22 reports the corresponding difference, $\Delta P_{loss,tot}$.

When AC losses are considered, the maximum total loss is approximately four times higher than in the case where AC losses are neglected, clearly demonstrating their impact on machine performance. Indeed, the absence of magnetic stator teeth guiding the flux lines leads to significantly increased AC losses in the stator copper windings. The highest total losses are observed in the HTS electrically excited synchronous machine, reaching values on the order of 160 kW in the high-torque, high-speed region. In contrast, the Halbach PM machine exhibits a lower maximum total loss, approximately 110 kW, under comparable operating conditions.

Consistently, with the efficiency analysis, the total loss difference map highlights operating regions in which the Halbach solution becomes competitive, particularly in the high-power region and around the rated operating point. While the HTS machine shows a clear advantage mainly in the medium-to-low torque and medium-to-high speed regions, owing to the possibility of reducing the air-gap flux density through rotor current control.

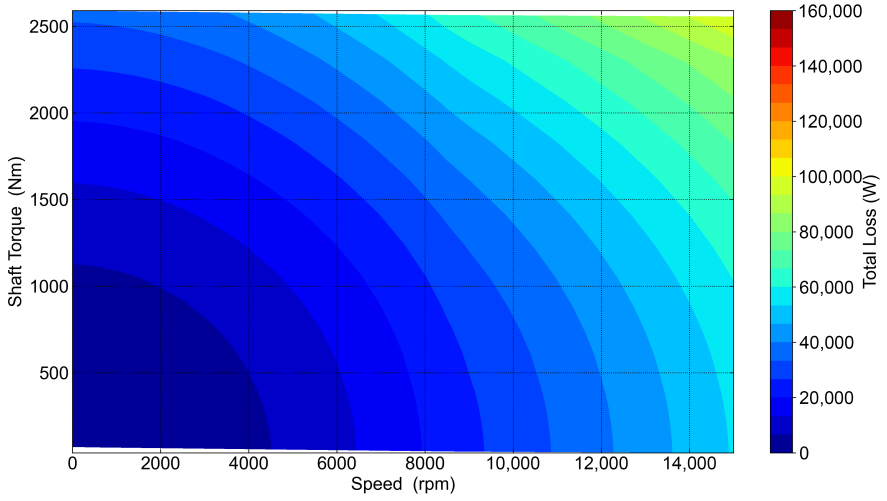


Figure 20. Total loss map of the Halbach PM machine including AC losses.

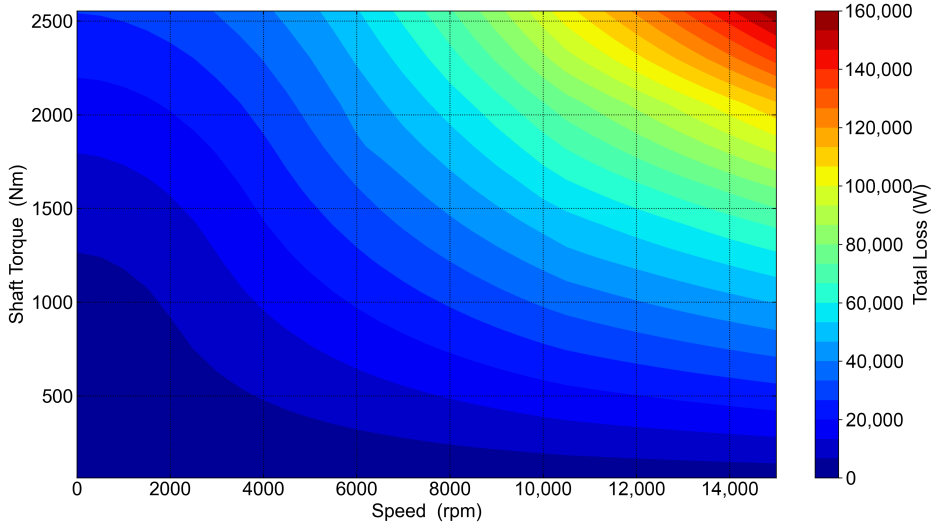


Figure 21. Total loss map of the HTS electrically excited synchronous machine including AC losses.

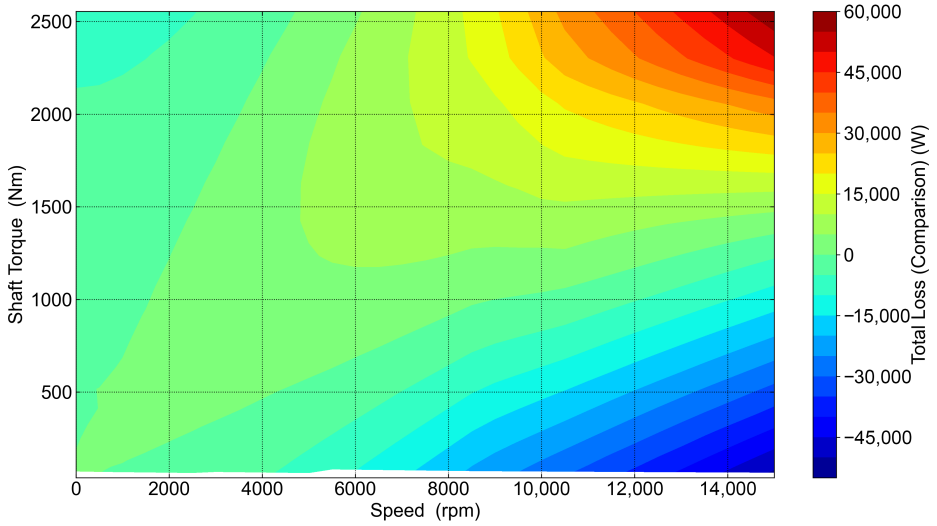


Figure 22. Total loss difference map, $\Delta P_{\text{loss,tot}} = P_{\text{loss,tot,SC}} - P_{\text{loss,tot,Halbach}}$ including AC losses.

4.8. DC Stator Copper (Joule) Losses Including AC Losses

Even when AC losses are included, further insight can be obtained by separately analyzing the two dominant loss components, the DC and AC stator copper losses. Given the significant contribution of copper losses under these conditions, the analysis of core losses is neglected, as their impact becomes comparatively negligible.

Figures 23 and 24 show the DC stator copper losses of the Halbach PM machine and the HTS electrically excited synchronous machine, respectively, while Figure 25 reports the corresponding loss difference.

As in the previous subsection, the DC stator copper losses are generally higher in the Halbach machine, owing to the same underlying reasons discussed earlier. However, a specific operating region can be identified in the medium-torque, high-speed area, where the DC stator copper losses are higher in the HTS electrically excited synchronous machine. This behavior is directly related to the adopted control strategy. In order to maximize efficiency, particularly by reducing AC losses, the optimal control requires a reduction in rotor current, which in turn necessitates a higher stator current compared with the previous operating condition. Consequently, the DC stator copper losses increase in this region.

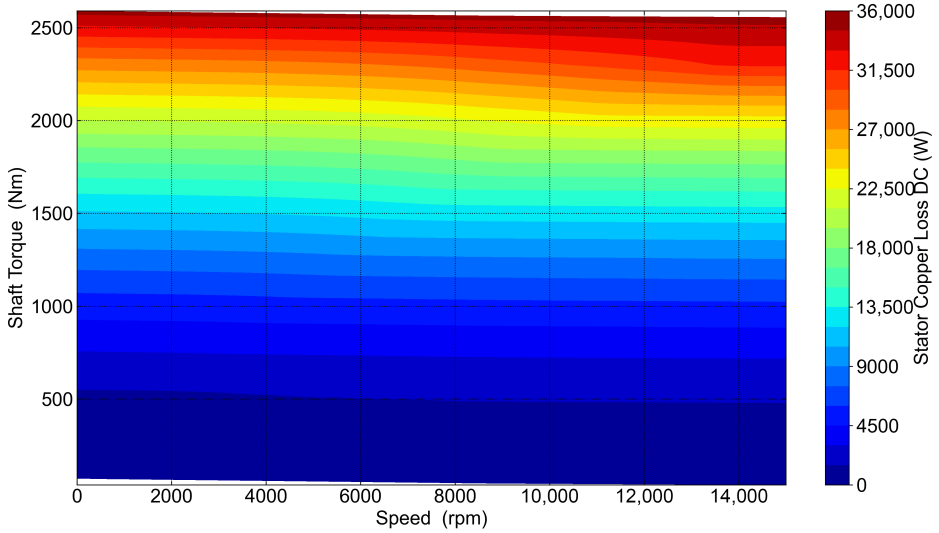


Figure 23. DC Stator copper (Joule) loss map of the Halbach PM machine including AC losses.

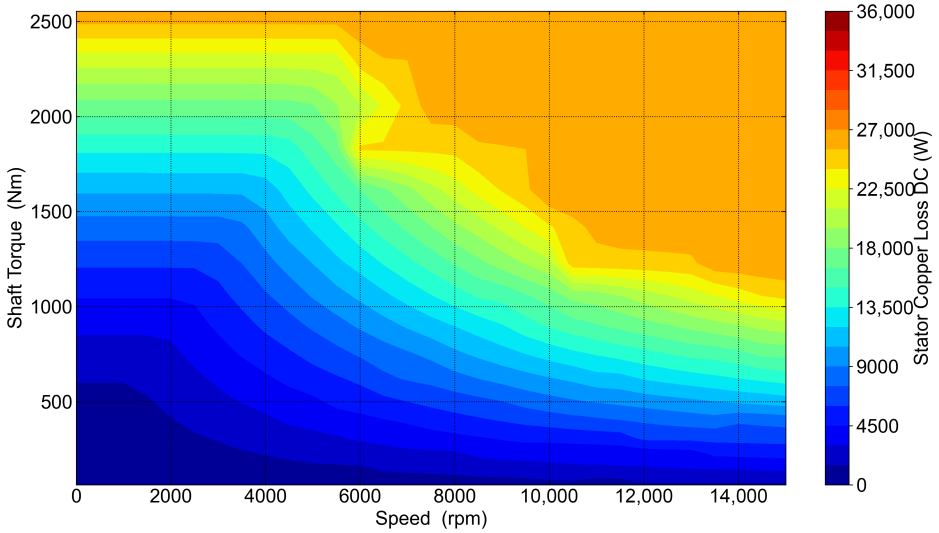


Figure 24. DC Stator copper (Joule) loss map of the HTS electrically excited synchronous machine.

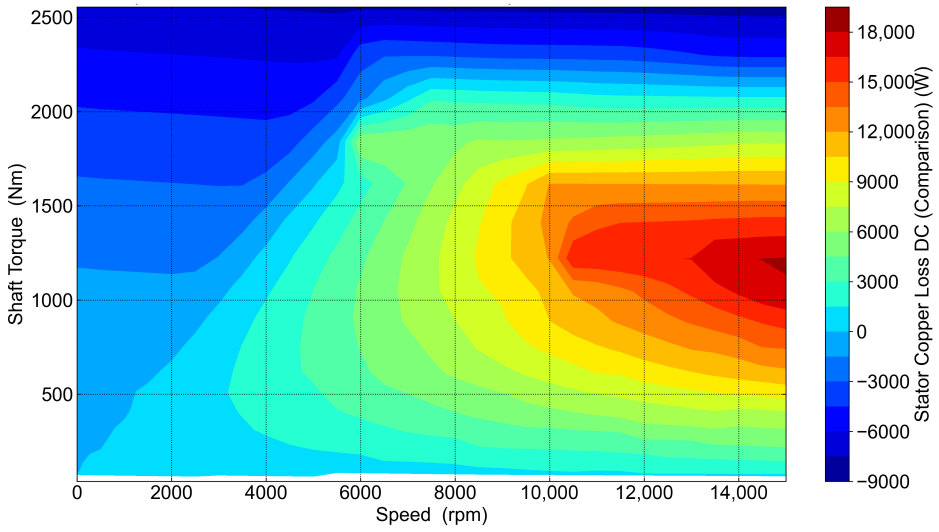


Figure 25. DC Copper loss difference map, $\Delta P_{\mathrm{Cu,DC}} = P_{\mathrm{Cu,DC,SC}} - P_{\mathrm{Cu,DC,Halbach}}$ including AC losses.

4.9. AC Stator Copper (Joule) Losses

The effects described above are illustrated in Figures 26–28, which present the AC stator copper losses of the Halbach PM machine and the HTS electrically excited synchronous machine, as well as their corresponding difference, respectively.

The AC-loss mapping was performed by means of a hybrid model calibrated against a full-FEA model at four representative operating points: maximum speed and maximum torque, maximum speed and 50% torque, 50% speed and 75% torque, and 50% speed and 25% torque. The calibration procedure showed that a single adjustment coefficient could guarantee a maximum deviation of about 10% on these four points with respect to the full-FEA results. However, for the final map generation a more practical calibration choice was adopted, prioritizing the reduction of the error at the maximum-speed, maximum-torque point, which is also the design point and the most significant operating condition for the present comparison. This choice led to larger errors at the other calibration points, but it enabled a substantial reduction in the computational burden associated with full-FEA simulations while maximizing the reliability of the most relevant comparison point. End-winding AC effects were not included in the adopted AC-loss model.

The significant impact of AC losses on overall machine performance is clearly evident, particularly for the HTS electrically excited synchronous machine. In this case, the maximum AC stator copper losses reach approximately 130 kW, a value considerably higher than the total losses computed when AC losses are neglected. The impact is lower in the Halbach PM machine; however, it remains relevant and contributes noticeably to the overall efficiency reduction.

The capability of superconducting excitation systems to achieve higher air-gap flux density enables a potential reduction in machine dimensions. Nevertheless, careful design considerations aimed at minimizing stator copper AC losses are essential. Otherwise, the increased AC losses may become critical, not only in terms of efficiency degradation but also with respect to the requirements and constraints of the cooling system.

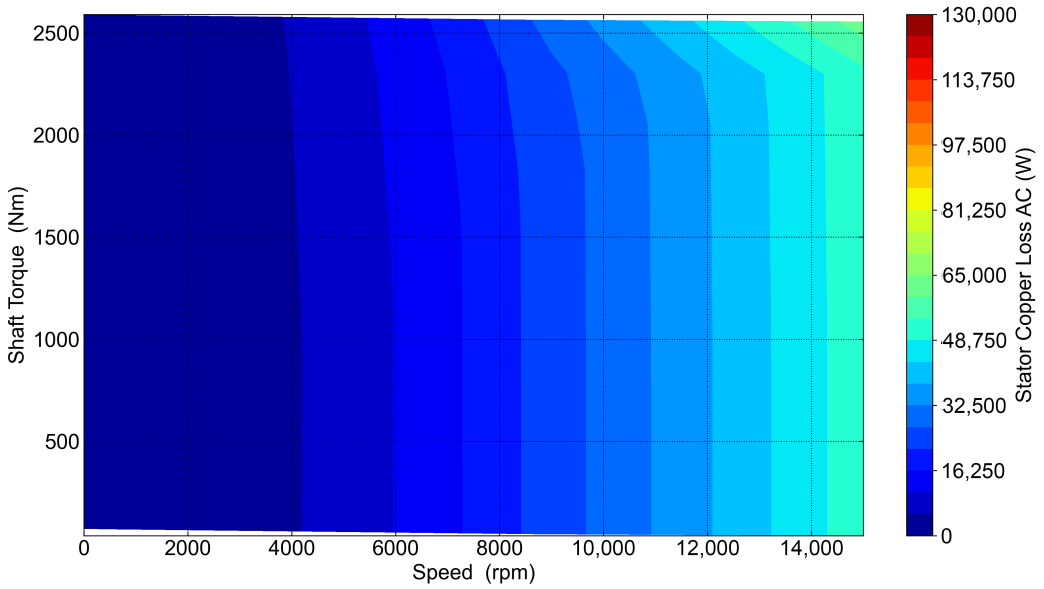


Figure 26. AC Stator copper (Joule) loss map of the Halbach PM machine including AC losses.

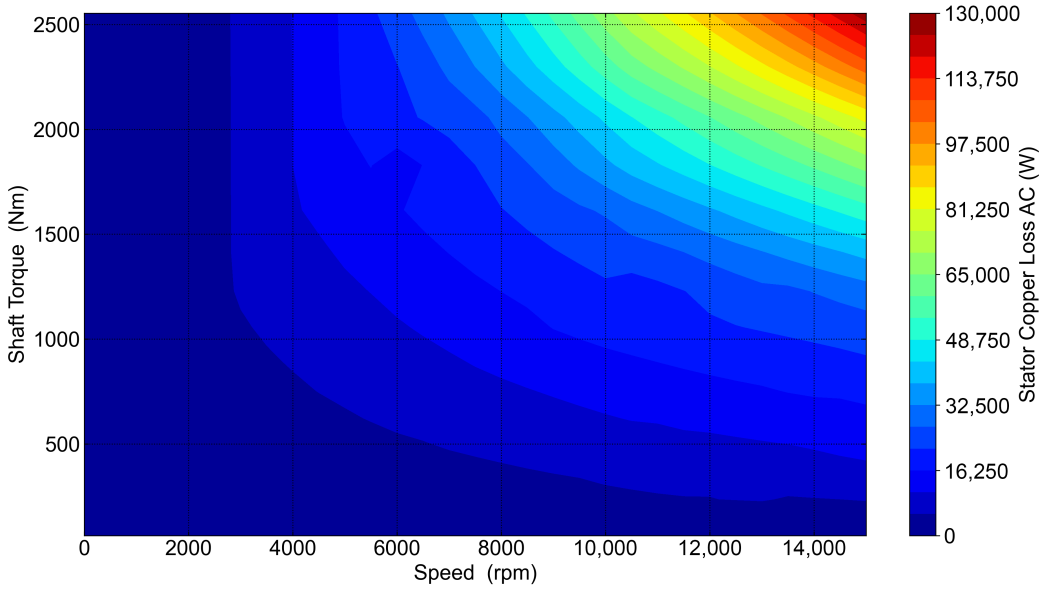


Figure 27. AC Stator copper (Joule) loss map of the HTS electrically excited synchronous machine.

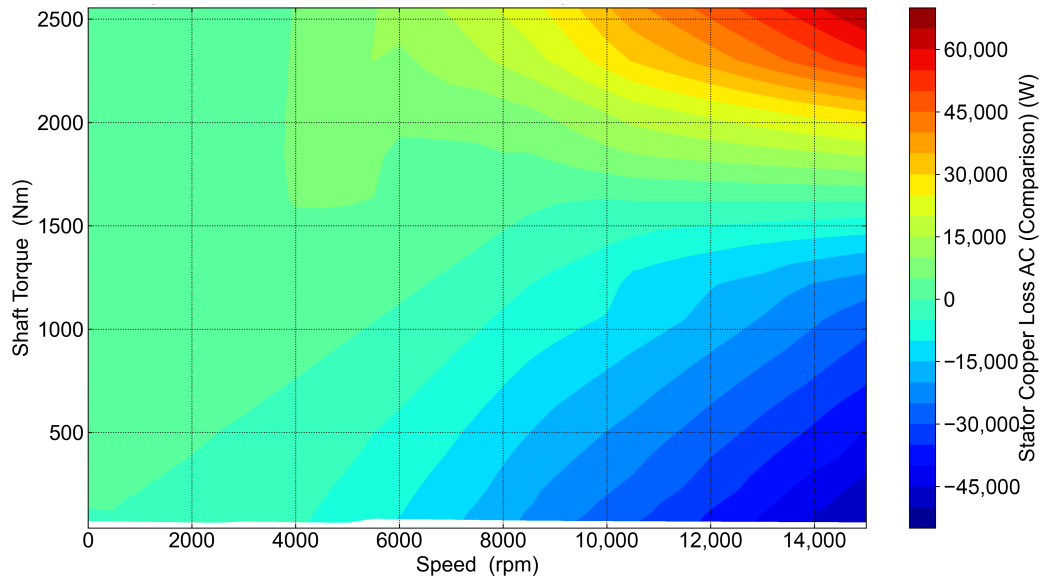


Figure 28. AC Copper loss difference map, $\Delta P_{\mathrm{Cu,AC}} = P_{\mathrm{Cu,AC,SC}} - P_{\mathrm{Cu,AC,Halbach}}$.

5. Conclusions

This article presented a comparative electromagnetic and performance assessment of two air-core, fault tolerant synchronous generators intended for high-power HE aircraft. A Halbach array PM synchronous generator constitutes the baseline design for a 4 MVA, 15,000 rpm application as representative of an already technologically mature solution. As a potential alternative, an electrically excited synchronous machine with HTS rotor winding is investigated, to increase the magnetic loading and reduce the active mass and volume. Both machines are equipped with a double three-phase stator winding to enhance redundancy and operational safety, and share the same stator cooling systems, ensuring the same electrical loading and a meaningful comparison. In addition, both machines have been analyzed within a consistent commercial simulation environment to generate the loss and efficiency maps and the performance indicators.

Neglecting the auxiliary subsystems (e.g., cooling and cryogenic apparatus), the HTS electrically excited synchronous machine demonstrates overall superior performance in

the high-power operating region, exhibiting lower total losses and a wider high-efficiency area compared to the Halbach array PM generator. Moreover, the HTS solution is lighter and more compact in terms of active parts, which represents a key advantage for aircraft applications, and presents intrinsic safety features relating to the controllability of the excitation current. A preliminary consideration of the cryogenic system also suggests that even when accounting for the additional mass associated with superconducting operation, the overall system mass can remain competitive with the permanent magnet solution. Furthermore, the lower electrical frequency of the HTS machine related to the low pole count simplifies the requirements on the power electronics, which is beneficial given the high current levels involved in megawatt-class aircraft generators. Nevertheless, the introduction of the SC technology in next-generation HE aircraft still requires significant advancements in the integration of cryogenic fluids in onboard systems, highlighting the maturity and commercialization advantage of the PM solution.

Author Contributions: Conceptualization, G.F. and A.T.; methodology, L.P., A.C. and F.G.; software, L.P. and A.C.; formal analysis, L.P., A.C. and F.G.; investigation, L.P. and A.C.; writing—original draft preparation, L.P. and A.C.; writing—review and editing, G.F., F.G., A.T. and S.V.; supervision, G.F. and A.T.; project administration, A.T.; funding acquisition, G.F. and A.T. All authors have read and agreed to the published version of the manuscript.

Funding: This study was carried out within the «Multi-phase fault tolerant MW range generation systems for hybrid electric aircraft (MUWGEN)» project—funded by European Union—Next Generation EU within the PRIN 2022 program (D.D. 104—02/02/2022 Ministero dell'Università e della Ricerca), as well as within the "Superconducting electric machines and crYogenic power electronics for high efficiency, reliable and power-dense eNERGY conversion (SYNERGY)" project—funded by European Union—Next Generation EU within the PRIN 2022 program (D.D. 104 02/02/2022 Ministero dell'Università e della Ricerca). This manuscript reflects only the authors' views and opinions and the Ministry cannot be considered responsible for them.

Data Availability Statement: The original contributions presented in this study are included in the article. Further inquiries can be directed to the corresponding author.

Conflicts of Interest: The authors declare no conflicts of interest.

References

1. Sarlioglu, B.; Morris, C.T. More Electric Aircraft: Review, Challenges, and Opportunities for Commercial Transport Aircraft. *IEEE Trans. Transp. Electrif.* **2015**, *1*, 54–64. [CrossRef]
2. da Silva, F.F.; Fernandes, J.F.P.; Branco, P.J.d.C. Barriers and Challenges Going from Conventional to Cryogenic Superconducting Propulsion for Hybrid and All-Electric Aircrafts. *Energies* **2021**, *14*, 6861. [CrossRef]
3. Cao, W.; Mecrow, B.C.; Atkinson, G.J.; Bennett, J.W.; Atkinson, D.J. Overview of Electric Motor Technologies Used for More Electric Aircraft (MEA). *IEEE Trans. Ind. Electron.* **2012**, *59*, 3523–3531.
4. Zhang, X.; Bowman, C.L.; O'Connell, T.C.; Haran, K.S. Large Electric Machines for Aircraft Electric Propulsion. *IET Electr. Power Appl.* **2018**, *12*, 767–779. [CrossRef]
5. Golovanov, D.; Gerada, D.; Xu, Z.; Gerada, C.; Page, A.; Sawata, T. Designing an Advanced Electrical Motor for Propulsion of Electric Aircraft. In Proceedings of the 2019 AIAA/IEEE Electric Aircraft Technologies Symposium (EATS), Indianapolis, IN, USA, 22–24 August 2019; pp. 1–12.
6. Chen, J.; Wang, C.; Chen, J. Investigation on the Selection of Electric Power System Architecture for Future More Electric Aircraft. *IEEE Trans. Transp. Electrif.* **2018**, *4*, 563–576.
7. Del Pizzo, A.; Di Noia, L.P.; Pizza, A. Analysis of a Five Phase Electrical Drive for the Propulsion of All Electric Aircraft. In Proceedings of the 2016 AEIT International Annual Conference (AEIT), Capri, Italy, 5–7 October 2016; pp. 1–6.
8. Sasa, H.; Iwakuma, M.; Yoshida, K.; Sato, S.; Sasayama, T.; Yoshida, T.; Yamamoto, K.; Miura, S.; Kawagoe, A.; Izumi, T.; et al. Experimental Evaluation of 1 kW-Class Prototype REBCO Fully Superconducting Synchronous Motor Cooled by Subcooled Liquid Nitrogen for E-Aircraft. *IEEE Trans. Appl. Supercond.* **2021**, *31*, 5200706. [CrossRef]
9. Barzkar, A.; Ghassemi, M. Components of Electrical Power Systems in More and All-Electric Aircraft: A Review. *IEEE Trans. Transp. Electrif.* **2022**, *8*, 4037–4053. [CrossRef]

10. Nøland, J.K.; Leandro, M.; Suul, J.A.; Molinas, M. High-Power Machines and Starter-Generator Topologies for More Electric Aircraft: A Technology Outlook. *IEEE Access* **2020**, *8*, 130104–130123.
11. Wheeler, P.; Bozhko, S. The More Electric Aircraft: Technology and Challenges. *IEEE Electrif. Mag.* **2014**, *2*, 6–12.
12. Sivasubramaniam, K.; Zhang, T.; Lokhandwalla, M.; Laskaris, E.T.; Bray, J.W.; Gerstler, B.; Shah, M.R.; Alexander, J.P. Development of a High Speed HTS Generator for Airborne Applications. *IEEE Trans. Appl. Supercond.* **2009**, *19*, 1656–1661. [CrossRef]
13. Golovanov, D.; Gerada, D.; Sala, G.; Degano, M.; Trentin, A.; Connor, P.H.; Xu, Z.; Rocca, A.L.; Galassini, A.; Tarisciotti, L.; et al. 4-MW Class High-Power-Density Generator for Future Hybrid-Electric Aircraft. *IEEE Trans. Transp. Electrif.* **2021**, *7*, 2952–2964. [CrossRef]
14. Ganev, E. Selecting the Best Electric Machines for Electrical Power-Generation Systems: High-Performance Solutions for Aerospace More Electric Architectures. *IEEE Electrif. Mag.* **2014**, *2*, 13–22. [CrossRef]
15. Haran, K.S.; Loder, D.; Deppen, T.O.; Zheng, L. Actively Shielded High-Field Air-Core Superconducting Machines. *IEEE Trans. Appl. Supercond.* **2016**, *26*, 98–105. [CrossRef]
16. Duran, M.J.; Barrero, F. Recent Advances in the Design, Modeling, and Control of Multiphase Machines—Part II. *IEEE Trans. Ind. Electron.* **2016**, *63*, 459–468. [CrossRef]
17. Jiang, X.; Huang, W.; Cao, R.; Hao, Z.; Jiang, W. Electric Drive System of Dual-Winding Fault-Tolerant Permanent-Magnet Motor for Aerospace Applications. *IEEE Trans. Ind. Electron.* **2015**, *62*, 7322–7330. [CrossRef]
18. Wang, J.; Qu, R.; Liu, Y.; Li, J. Study of Multiphase Superconducting Wind Generators with Fractional-Slot Concentrated Windings. *IEEE Trans. Appl. Supercond.* **2014**, *24*, 5202106. [CrossRef]
19. Barrero, F.; Duran, M.J. Recent Advances in the Design, Modeling, and Control of Multiphase Machines—Part I. *IEEE Trans. Ind. Electron.* **2016**, *63*, 449–458. [CrossRef]
20. Dai, B.; Xu, F.; Tan, Y.; Sun, J. Enhanced Continuous Terminal Sliding Mode Position Control for PMSM Servo Systems Considering Speed and Current Constraints. *IEEE Trans. Energy Convers.* **2026**, 1–11. [CrossRef]
21. Dai, B.; Wang, Z.; Zhao, J.; Li, S. Critical Current-Constrained Continuous Nonsingular Terminal Sliding Mode Control for PMSM Based on Control Barrier Function. *IEEE Trans. Power Electron.* **2025**, *40*, 15093–15103. [CrossRef]
22. Xiao, Y.; Lyu, X.; Zhang, J.; Yu, A.; Zheng, Y.; Wang, R. 1 MW-Class High-Speed Interior Permanent Magnet Synchronous Machines for Electrical Aviation Propulsion. *Electronics* **2026**, *15*, 1163. [CrossRef]
23. Zhou, Y.; Su, H.; Yu, S.; Li, W.; Wang, Y.; Zhao, Y.; He, Y.; Dai, Y. Design and Testing of Warm Rotor for a 200 kW High-Temperature Superconducting Generator. *IEEE Trans. Appl. Supercond.* **2024**, *34*, 5204005. [CrossRef]
24. Iwakuma, M.; Tomioka, A.; Konno, M.; Hase, Y.; Satou, T.; Iijima, Y.; Saitoh, T.; Yamada, Y.; Izumi, T.; Shiohara, Y. Development of a 15 kW Motor with a Fixed YBCO Superconducting Field Winding. *IEEE Trans. Appl. Supercond.* **2007**, *17*, 1607–1610. [CrossRef]
25. Scheidler, J.; Tallerico, T. Methodology for Electromagnetic Optimization of a Partially Superconducting 1.4 MW Electric Machine for Electrified Aircraft Propulsion. *IEEE Trans. Appl. Supercond.* **2023**, *33*, 5202405. [CrossRef]
26. Bailey, W.; Wen, H.; Al-Mosawi, M.; Goddard, K.; Yang, Y. Testing of a Lightweight Coreless HTS Synchronous Generator Cooled by Subcooled Liquid Nitrogen. *IEEE Trans. Appl. Supercond.* **2011**, *21*, 1159–1162. [CrossRef]
27. Moon, H.; Kim, Y.-C.; Park, H.-J.; Park, M.; Yu, I.-K. Development of a MW-Class 2G HTS Ship Propulsion Motor. *IEEE Trans. Appl. Supercond.* **2016**, *26*, 5203805. [CrossRef]
28. Terao, Y.; Sekino, M.; Ohsaki, H. Electromagnetic Design of 10 MW Class Fully Superconducting Wind Turbine Generators. *IEEE Trans. Appl. Supercond.* **2012**, *22*, 5201904. [CrossRef]
29. Wang, J.; Qu, R.; Liu, Y. Comparison Study of Superconducting Generators with Multiphase Armature Windings for Large-Scale Direct-Drive Wind Turbines. *IEEE Trans. Appl. Supercond.* **2013**, *23*, 5201005. [CrossRef]
30. Kalsi, S.S. Advances in Synchronous Machines Employing High Temperature Superconductors (HTS). In Proceedings of the IEEE International Electric Machines and Drives Conference, 2003, IEMDC'03, Madison, WI, USA, 1–4 June 2003; Volume 1, pp. 24–28.
31. Balachandran, T.; Lee, D.; Salk, N.; Haran, K.S. A Fully Superconducting Air-Core Machine for Aircraft Propulsion. *IOP Conf. Ser. Mater. Sci. Eng.* **2020**, *756*, 012030. [CrossRef]
32. Madonna, V.; Giangrande, P.; Galea, M. Electrical Power Generation in Aircraft: Review, Challenges, and Opportunities. *IEEE Trans. Transp. Electrif.* **2018**, *4*, 646–659. [CrossRef]
33. Luongo, C.A.; Masson, P.J.; Nam, T.; Mavris, D.; Kim, H.D.; Brown, G.V.; Waters, M.; Hall, D. Next Generation More-Electric Aircraft: A Potential Application for HTS Superconductors. *IEEE Trans. Appl. Supercond.* **2009**, *19*, 1055–1068. [CrossRef]
34. Tenconi, A.; Crescimbini, F.; Tursini, M.; Tani, A.; Jiménez Molina, M.; Vita, L.; Credo, A.; Bellini, A.; Perilli, L.; Fabri, G.; et al. Multi-Phase Fault Tolerant MW Range Synchronous Machine Drives for Hybrid-Electric Aircraft. In Proceedings of the 2024 IEEE International Conference on Electrical Systems for Aircraft, Railway, Ship Propulsion and Road Vehicles & International Transportation Electrification Conference (ESARS-ITEC), Naples, Italy, 26–29 November 2024; pp. 1–7.
35. Abrahamsen, A.B.; Mijatovic, N.; Seiler, E.; Sorensen, M.P.; Koch, M.; Norgard, P.B.; Pedersen, N.F.; Traeholt, C.; Andersen, N.H.; Ostergard, J. Design Study of 10 kW Superconducting Generator for Wind Turbine Applications. *IEEE Trans. Appl. Supercond.* **2009**, *19*, 1678–1682. [CrossRef]

36. Shafaie, R.; Kalantar, M. Design of a 10-MW-Class Wind Turbine HTS Synchronous Generator with Optimized Field Winding. *IEEE Trans. Appl. Supercond.* **2013**, *23*, 5202307. [CrossRef]
37. Fukui, S.; Ogawa, J.; Sato, T.; Tsukamoto, O.; Kashima, N.; Nagaya, S. Study of 10 MW-Class Wind Turbine Synchronous Generators with HTS Field Windings. *IEEE Trans. Appl. Supercond.* **2011**, *21*, 1151–1154. [CrossRef]
38. Graffeo, F.; Vaschetto, S.; Tenconi, A.; Cavagnino, A. Fast Sizing Procedure for Salient-Pole Wound Field Synchronous Motors for Transportation Electrification. In Proceedings of the 2023 IEEE International Electric Machines & Drives Conference (IEMDC), San Francisco, CA, USA, 15–18 May 2023; pp. 1–7.
39. Pyrhonen, J.; Jokinen, T.; Hrabovcova, V. *Design of Rotating Electrical Machines*, 2nd ed.; John Wiley & Sons: Hoboken, NJ, USA, 2013.
40. Safi, S.K.; Bumby, J.R. Analysis of Magnetic Fields in the Slotted Structure of a Superconducting AC Generator. *IEE Proc. C Gener. Transm. Distrib.* **1992**, *139*, 411–422. [CrossRef]
41. Zhang, W.; Xia, D.; Zhang, D.; Zhang, G. Parameter Design by a Novel Method and Optimization of the Field Coil for a 500 kW Air-Gap HTS Generator. *IEEE Trans. Appl. Supercond.* **2014**, *24*, 5201704. [CrossRef]
42. Hughes, A.; Miller, T.J.E. Analysis of Fields and Inductances in Air-Cored and Iron-Cored Synchronous Machines. *Proc. Inst. Electr. Eng.* **1977**, *124*, 121–126. [CrossRef]
43. Miyazaki, H.; Iwakuma, M.; Emori, Y.; Sasa, H.; Yoshida, K.; Sato, S.; Miura, S.; Sagara, I.; Suzuki, Y.; Konno, M.; et al. Fabrication and Test of a 400 kW-Class Fully Superconducting Synchronous Motor Using REBCO Tape for an Electric Propulsion System. *IEEE Trans. Appl. Supercond.* **2024**, *34*, 5200506. [CrossRef]
44. Parma, V. Cryostat Design. *arXiv* **2014**, arXiv:1501.07154.
45. Huber, F.; Song, W.; Zhang, M.; Grilli, F. The T-A Formulation: An Efficient Approach to Model the Macroscopic Electromagnetic Behaviour of HTS Coated Conductor Applications. *Supercond. Sci. Technol.* **2022**, *35*, 043003. [CrossRef]
46. Ye, J.; Li, G.-J. 10 MW Direct-Drive Superconducting Vernier Machines for Offshore Wind Power Application. In Proceedings of the 2025 IEEE International Electric Machines & Drives Conference (IEMDC), Houston, TX, USA, 18–21 May 2025; pp. 1222–1227.
47. Sun, W.; Wang, L.; Wang, Q. Fabrication of Racetrack-Type Double-Pancake Coils Using 2G Tapes and Online Mechanical Shock Test. *Phys. C Supercond. Its Appl.* **2023**, *610*, 1354271. [CrossRef]
48. Komiya, M.; Aikawa, T.; Sasa, H.; Miura, S.; Iwakuma, M.; Yoshida, T.; Sasayama, T.; Tomioka, A.; Konno, M.; Izumi, T. Design Study of 10 MW REBCO Fully Superconducting Synchronous Generator for Electric Aircraft. *IEEE Trans. Appl. Supercond.* **2019**, *29*, 5204306. [CrossRef]
49. Nilsson, E.; Rivenc, J.; Rouquette, J.F.; Tassisto, M.; Fallouh, C.; Ybanez, L.; Dönges, S.A.; Weiss, J.; Radcliff, K.; van der Laan, D.; et al. Performance of the 500 kW Superconducting DC and AC Links of the ASCEND Demonstrator at Airbus. *IEEE Trans. Appl. Supercond.* **2024**, *34*, 4801704. [CrossRef]
50. Hartmann, C.; Nøland, J.K.; Nilssen, R.; Mellerud, R. Dual Use of Liquid Hydrogen in a Next-Generation PEMFC-Powered Regional Aircraft with Superconducting Propulsion. *IEEE Trans. Transp. Electrif.* **2022**, *8*, 4760–4778. [CrossRef]

Disclaimer/Publisher's Note: The statements, opinions and data contained in all publications are solely those of the individual author(s) and contributor(s) and not of MDPI and/or the editor(s). MDPI and/or the editor(s) disclaim responsibility for any injury to people or property resulting from any ideas, methods, instructions or products referred to in the content.